https://doi.org/10.5194/essd-2026-193
Preprint. Discussion started: 26 May 2026

Open Access Earth System Science Data Discussions

A pan-tropical 5-km monthly L-band vegetation optical depth dataset from pan-sharpening-based downscaling

Jinan Shi[1], Jiaxin Li[4], Lianru Gao[5], Siyu Liu[6], Rasmus Fensholt[6], Philippe Ciais[7], Xiaojun Li[8], Qiangqiang Yuan[9], Jean-Pierre Wigneron[10], Lei Fan[2,3]

[1]School of Mathematical and Physical Sciences, Chongqing University of Science and Technology, Chongqing, 401331, China
[2]Chongqing Jinfo Mountain Karst Ecosystem National Observation and Research Station, School of Geographical Sciences, Southwest University, Chongqing 400715, China
[3]Chongqing Engineering Research Center for Remote Sensing Big Data Application, School of Geographical Sciences, Southwest University, Chongqing 400715, China
[4]School of Computer Science and Technology, Chongqing University of Posts and Telecommunications, Chongqing, 400065, China
[5]Key Laboratory of Computational Optical Imaging Technology, Aerospace Information Research Institute, Chinese Academy of Sciences, Beijing, 100094, China.
[6]Department of Geosciences and Natural Resource Management, University of Copenhagen, Copenhagen 1350, Denmark
[7]Laboratoire des Sciences du Climat et de l'Environnement, LSCE/IPSL, CEA-CNRS-UVSQ, Université Paris Saclay, Gif-sur-Yvette 91191, France
[8]Faculty of Geosciences and Engineering, Southwest Jiaotong University, Chengdu, 611756, China
[9]School of Geodesy and Geomatics, Wuhan University, Wuhan, 430079, China
[10]ISPA, UMR 1391, INRAE Nouvelle-Aquitaine, Université de Bordeaux, Villenave d'Ornon F-33140, France

Correspondence to: Lei Fan (leifan33@swu.edu.cn)

Abstract. L-band Vegetation optical depth (L-VOD), as a microwave-derived vegetation indicator, has been widely applied in the monitoring of vegetation dynamics. However, the spatial resolution of 25-km or coarser in existing L-band VOD products limits their applications in ecological monitoring requiring a higher level of spatial details. To mitigate this limitation, we introduce a pan-sharpening-based downscaling method to improve the spatial resolution of L-VOD. By fusing the spatial structural features of the aggregated 5-km resolution European Space Agency Climate Change Initiative (ESA CCI) aboveground biomass (AGB) product, the SMOS L-VOD product over tropical regions was downscaled to generate a monthly 5-km resolution L-VOD dataset spanning 2015 to 2021. The downscaling model demonstrated high accuracy, with a correlation coefficient (R) of 0.95 and a root mean square error ($RMSE$) of 0.11 when comparing the simulated 25-km L-VOD ($L-VOD_{25km}^{sim}$) with the original L-VOD ($L-VOD_{25km}$) product. Spatially, the 5-km resolution L-VOD ($L-VOD_{5km}$) yielded a strong correlation with above-ground biomass ($R = 0.91$, R^2 =0.86), and temporally dynamics, it accurately characterized the LAI variations of short vegetation and forest area loss at the pixel level over the study period. The results demonstrate that our downscaling method can effectively enhance the spatial resolution of L-VOD while preserving its original spatiotemporal dynamics, and is capable of capturing forest disturbance. This dataset can be downloaded at https://doi.org/10.11888/RemoteSen.tpdc.303391 (Shi and Fan, 2026).

Keywords: L-band Vegetation Optical Depth (L-VOD), Downscaling, Pan-sharpening, Pan-tropical, 5-km resolution

https://doi.org/10.5194/essd-2026-193
Preprint. Discussion started: 26 May 2026

1 Introduction

Vegetation optical depth (VOD) provides critical insights into the dynamics of the global carbon in the context of changing environmental and climatic conditions (Skulovich et al., 2024). It provides reliable estimates of vegetation biomass (Yang et al., 2023; Wigneron et al., 2024; Zhang et al., 2025; Tong et al., 2020) and vegetation water content (VWC) (Felton et al., 2025; Jackson and Schmugge, 1991; Piles et al., 2017; Tong et al., 2018), based on the parameterization of vegetation attenuation and emission (Wigneron et al., 2017). Global long-term time-series VOD products can be obtained from various active and passive observations at different microwave frequency bands, such as C-band (Liu et al., 2021; Liu et al., 2023; Owe et al., 2008), X-band (Karthikeyan et al., 2019; Wang et al., 2021), and L-band (Chaubell et al., 2021; Konings et al., 2016; Wigneron et al., 2021). L-band exhibits greater penetration capability through the vegetation canopy than C-band and X-band, and thus shows a considerably lower saturation effect compared with other frequencies (Xing et al., 2024), particularly where vegetation canopy is dense and biomass density is high (Brandt et al., 2018). Therefore, L-VOD provides a more reliable means of monitoring forest structural properties and their temporal dynamics in high-biomass regions. Two currently operational L-band missions – Soil Moisture and Ocean Salinity (SMOS) (Kerr et al., 2010) and Soil Moisture Active Passive (SMAP) (Entekhabi et al., 2008; Xing et al., 2024) – have shown a strong capability for monitoring both the vegetation and soil dynamics globally (Wigneron et al., 2017). Many L-VOD datasets have been generated in recent years, offering reliable and dependable long-term L-band VOD time series for use in ecological and climate-related analyses. A range of distinct datasets are known as SMOS-IC (Fernandez-Moran et al., 2017), SMAP-IB (Li et al., 2022a; Xiao et al., 2024), SMOSMAP-IB (Li et al., 2022b), SMAPMT-DCA (Konings et al., 2017) and VODCA v2 (Zotta et al., 2024).

Although satellite-based VOD retrievals provide essential regional to continental-scale forest biomass information at daily temporal resolution, their coarse spatial resolution (≥25-km) limits their application to accurately monitor local, fine-scale, or patchy forest biomass dynamics. At such coarse resolution, each grid cell typically encompasses multiple land cover types, which prevents investigations into the temporal dynamics of diverse vegetation categories (Vreugdenhil et al., 2020). Moreover, for each VOD pixel, the properties of the microwave signal are significantly influenced the following factors: the density of the vegetation, the roughness features of the soil surface, together with the VWC (Piles et al., 2009; Zhou et al., 2022), which leads to exceptionally strong spatial variability of VOD within individual pixels (Owe et al., 2002). Additionally, higher-resolution VOD serves as a critical parameter in microwave radiative transfer models for soil moisture (SM) retrievals, while further contributing prominently to higher-resolution SM inversion (Vreugdenhil et al., 2020). Thus, higher-resolution VOD is becoming increasingly crucial for vegetation dynamics monitoring and hydrological studies at regional and local level. Additionally, it offers the possibility of filling gaps in optical vegetation indices (VIs) that are unavailable in the presence of cloud cover.

Researchers have employed both passive and active microwave radiation to retrieve higher-resolution VOD. For passive retrieval, the Land Parameter Retrieval Model (LPRM) has been applied to sharpened AMSR-E brightness temperatures, yielding soil moisture and VOD at an enhanced resolution of approximately 10-km across Australia (Gevaert et al., 2016).

https://doi.org/10.5194/essd-2026-193
Preprint. Discussion started: 26 May 2026

Active microwave sensors and especially SARs are capable of offering far higher spatial resolutions than passive radiometers (Peng et al., 2017; Liu et al., 2023). C-band backscatter data acquired by Sentinel-1 have been utilized to retrieve VOD products with a spatial resolution of 1-km (El Hajj et al., 2019; Zhou et al., 2022). However, retrieving VOD from SAR is often difficult as a result of the integrated influences of canopy architecture, surface roughness, and moisture content on SAR backscatter (Wagner et al., 2007; Frappart et al., 2020).

Statistical downscaling, which is also referred to as multi-parameter fusion-based downscaling (Jing et al., 2022), introduces higher resolution auxiliary parameters and fuses them with the coarse-resolution VOD data to obtain the finer resolution VOD data. The core of these methods lies in developing a statistical model of the VOD-auxiliary variable relationship at a low resolution. This model is subsequently applied to generate high-resolution estimates, based on the key assumption that the relationship does not vary with spatial scale (Jing et al., 2022). In terms of auxiliary data sources, in one respect, scholars have utilized active microwave auxiliary data (Jiang et al., 2024) and proposed VOD downscaling methods using radar backscatter coefficients (Bousquet et al., 2019). In another respect, investigators have applied optical or thermal infrared auxiliary data (Jiang et al., 2024) and developed downscaling approaches to estimate VOD, such as based on vegetation indices NDVI (Xinyu et al., 2025). The conventional statistical approaches discussed above are subject to the limitation of the assumption of linearity between VOD and auxiliary variables, consequently failing to capture their complex nonlinear interactions.

Previous studies have utilized random forest (RF) models to downscale VOD with multi-source auxiliary information. The downscaling of VOD using RF firstly builds up a relationship between low-resolution VOD and higher-resolution vegetation indices (e.g., NDVI, LAI), and subsequently the relationship is used to convert higher-resolution vegetation indices into higher-resolution VOD. This means that the estimated higher-resolution VOD can be considered to be a conversion of vegetation indices values. For instance, previous studies (Mohite et al., 2022; Yan et al., 2025) used RF to downscale VOD, by building up the relationship between VOD and LST, NDVI, DEM.

In the aforementioned VOD downscaling methods, the auxiliary higher-resolution variables include optical vegetation indices like NDVI (Mohite et al., 2022; Xinyu et al., 2025; Yan et al., 2025) and radar data (e.g., L-band backscattering coefficients from the ALOS-1 mission) (Bousquet et al., 2019). NDVI exhibits significant saturation phenomena in regions with high vegetation coverage (Xinyu et al., 2025), while L-band radar backscatter coefficients (HV polarization) typically demonstrate signal saturation in evergreen broadleaf forests when exceeding 0.07 (Bousquet et al., 2019). Although L-VOD and AGB exhibit an obvious non-linear saturating relationship, the degree of saturation is relatively weak (Li et al., 2021). Furthermore, the Climate Change Initiative (CCI) AGB product provides 100 m resolution data (derived from multi-source fusion and spatial resampling (Boitard et al., 2024), making CCI-AGB a suitable high-resolution auxiliary variable for image fusion-based downscaling methods to enhance spatial detail representation.

An alternative downscaling method based on the morphological filtering-based multiresolution analysis (MF-MRA) technique (Restaino et al., 2016) uses 5-km resolution AGB data to sharpen the low-resolution VOD data. This method utilizes the VOD as a baseline, employing morphological operators to extract spatial structural features—such as textural and edge

https://doi.org/10.5194/essd-2026-193
Preprint. Discussion started: 26 May 2026

information—from the AGB data, and injects them into the VOD. Consequently, the method could improve spatial resolution through structural feature injection, without relying on the absolute values of auxiliary data.

Within the present work, we adopt the MF-MRA fusion approach commonly used in panchromatic sharpening to enhance the spatial resolution of L-VOD. By fusing the monthly 25-km resolution L-VOD data with the concurrent monthly 5-km resolution aggregated ESA CCI AGB (original 100-m resolution) from 2015 to 2021, a monthly 5-km resolution L-VOD dataset for the period 2015–2021 is generated. This strategy not only improves the spatial resolution of the L-VOD product but also effectively preserves the potential nonlinear structural information between L-VOD and AGB in the fusion process.

The primary aims of this work are as follows: (1) to introduce a novel L-VOD downscaling framework, which is based on MF-MRA to enhance the spatial resolution of SMOS-IC L-VOD from 25-km to 5-km, (2) to demonstrate the applicability and robustness of the proposed downscaling approach, and (3) to validate the spatiotemporal consistency of the downscaled L-VOD in regards to temporal variation and spatial distribution. This was done through comparisons with AGB, LAI, and forest loss datasets.

2 Datasets

2.1 Study area and land cover

Our study focused on the tropical region spanning 25° N to 25° S (Fig. 1), covering tropical America, Africa, and Asia. This region contains the world's major rainforests, which are characterized by greater rainfall and denser vegetation than other regions (Ma et al., 2023). These forests are dynamic ecosystems that undergo ecological succession, natural perturbations, deforestation, and land degradation (Abbas et al., 2020), and provide more than half the uptake of terrestrial atmospheric carbon dioxide (CO_2) (Stephens et al., 2007; Lewis et al., 2009). The spatial heterogeneity in both climate and vegetation types makes this region ecologically representative and suitable for a large-scale study on downscaling L-VOD.

Land cover data for this study were derived from the MODIS MCD12C1 dataset (Friedl et al., 2010), which offers 5-km resolution land cover classifications for 2019 following the International Geosphere-Biosphere Programme (IGBP) scheme. We performed an aggregation at a 25-km grid resolution using the predominant category. "Predominant" denotes the class with the highest frequency of 5-km pixels within each 25-km grid.

https://doi.org/10.5194/essd-2026-193
Preprint. Discussion started: 26 May 2026

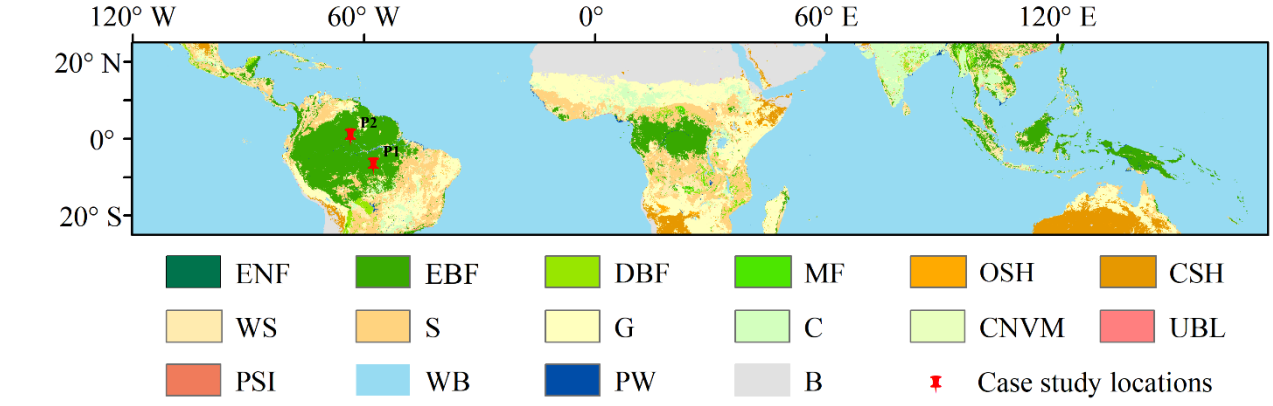

Figure 1. The land cover categories for 2019 over the tropical study domain are obtained from the MODIS dataset at 5-km spatial resolution. Deciduous needleleaf forest (DNF), Evergreen broadleaf forest (EBF), Evergreen needleleaf forest (ENF), Mixed forests (MF), Closed Shrublands (CSH), Open Shrublands (OSH), Woody Savannas (WS), Savannas (S), Grasslands (G), Permanent Wetlands (PW), Croplands (C), Cropland/Natural Vegetation Mosaics (CNVM), Barren (B). The two detailed study regions (P1 and P2), each comprising a 2×2 group of Soil Moisture and Ocean Salinity (SMOS) grid cells (P1: central latitude, 7.0° S; longitude, 57.5° W; P2: central latitude, 0.53° N; longitude, 63.43° W) are shown in Fig. 6 and Fig. 10.

2.2 L-VOD product

The L-VOD was retrieved from SMOS satellite descending and ascending orbit observations via the SMOS-IC algorithm, covering the period from 2010–2021 (Li et al., 2020). Radio frequency interference (RFI) can distort the signals received by satellite sensors, potentially introducing uncertainty into the VOD retrieval process. L-VOD data affected by RFI were excluded utilizing the methodology described by Wigneron et al. (2021), which applies a threshold of 8 K to the root mean square error ($RMSE$) between measured and simulated brightness temperature. Furthermore, bilinear interpolation, commonly used in VOD processing (Li et al., 2021; Liu et al., 2018), was applied to reproject and resample the L-VOD dataset to a 25-km grid. For this study, L-VOD data for the period 2015–2021 were utilized.

2.3 AGB

AGB estimates in the ESA CCI Biomass maps (Santoro and Cartus, 2024) are based on radar backscatter intensity measurements. According to Boitard et al. (2024), these measurements were obtained from the PALSAR2 sensor onboard ALOS2 and the Sentinel-1 satellites, which were developed under the ESA CCI Biomass project. LiDAR metrics and surface reflectance were also used in the estimation procedure. These AGB maps are updated on an annual basis and have a spatial resolution of 100 x100m. This work uses version 5.01 of the maps for the period 2015–2021. The original 100-m resolution AGB maps were aggregated to a 5-km resolution using mean values to serve as input for the downscaling model.

2.4 MODIS Vegetation Indices

NDVI and LAI, which are frequently adopted as proxies for green vegetation coverage (Grant et al., 2016; Lawrence et al., 2014; Liu et al., 2011; Liu et al., 2021) were used to assess the performance of downscaled L-VOD. The MOD13A1 Version

https://doi.org/10.5194/essd-2026-193
Preprint. Discussion started: 26 May 2026

6.0 dataset provides 16-day composite NDVI records at a spatial resolution of 500-m, derived by selecting and averaging the highest-quality observations during each 16-day compositing period (Didan, 2015). The MODIS MOD15A2H Version 6 dataset provides 8-day averaged LAI values on a 500-m spatial grid (Myneni et al., 2015). Over the study period, high-quality NDVI and LAI pixels flagged by the quality control layers were chosen and resampled to a 5-km spatial grid using an averaging method.

2.5 Forest Cover Loss

Hansen et al. (2013) developed a forest cover loss dataset (version 1.11) that maps annual forest loss at a 30-m spatial grid for the 2000–2023 period. In this product, forest cover loss is defined as temporary or permanent transition from forest to nonforest. This dataset includes a "lossyear" layer that denotes the year of detected forest cover loss, covering all forest loss events observed from 2000 to 2023 (Fan et al., 2022). Here, annual forest percentage loss rates over the period 2015–2021 were computed based on the resolution of downscaled L-VOD grid. Specifically, we quantified the proportion of the total forest loss areas as identified in the "lossyear" within each downscaled L-VOD grid cell (~5-km). Of note, this forest loss product represents temporary or permanent tree cover loss resulting from disturbances such as wildfires or clearcutting.

2.6 Canopy Height

We used a global forest canopy height (CH) product at 30-m resolution for 2019, produced by the Global Land Analysis and Discovery team at the University of Maryland (UMD GLAD) (Potapov et al., 2021), which provides seamless coverage from 52°N to 52°S latitudes. To align with the spatial scale employed in this research, the original dataset was aggregated to 5-km by averaging.

3 Methods

Fig. 2 presents the flow chart of our sequential downscaling process, consisting of three steps: (1) data preparation, (2) downscaling, and (3) evaluation.

https://doi.org/10.5194/essd-2026-193
Preprint. Discussion started: 26 May 2026

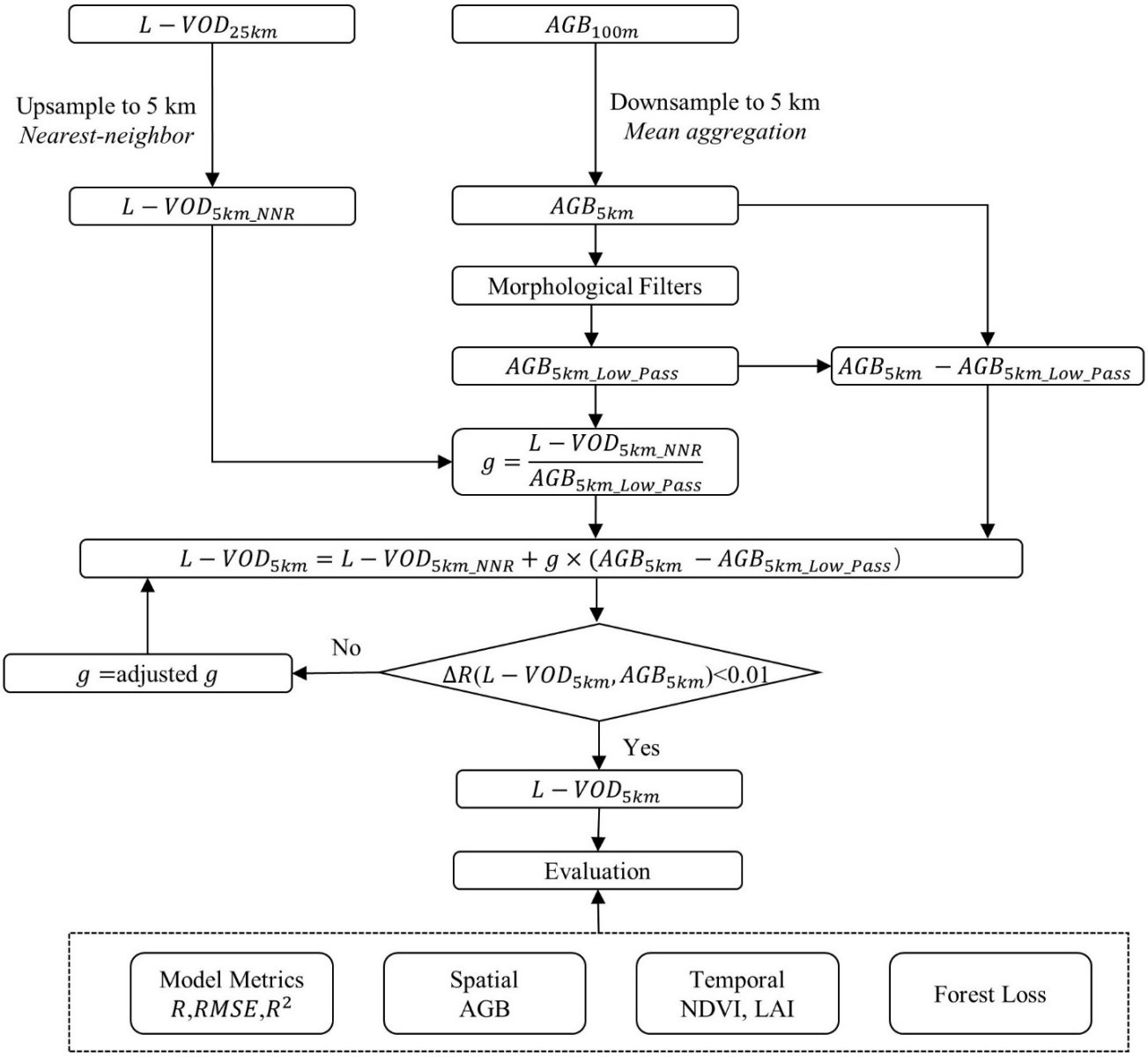

Figure 2. Flowchart illustrating the workflow for generating and validating downscaled L-VOD products.

3.1 Data preparation

We adopted the 25-km resolution L-VOD and the 100-m resolution AGB as inputs, namely $L-VOD_{25km}$ and AGB_{100m} in Fig. 2, respectively. The AGB data provided higher-resolution spatial details to guide the enhancement of L-VOD resolution. The monthly $L-VOD_{25km}$ data from 2015 to 2021 were first combined into 12-band images for each year. The L-VOD were then resampled to 5-km resolution ($L-VOD_{5km\_NNR}$) through the nearest-neighbor resampling (NNR) approach, which avoids

https://doi.org/10.5194/essd-2026-193
Preprint. Discussion started: 26 May 2026

Open Access Earth System Science Data Discussions

interpolation-based smoothing and preserves the fidelity of the original data (Parker et al., 2007; Porwal and Katiyar, 2014). AGB_{100m} data were aggregated to 5-km resolution (AGB_{5km}) through arithmetic averaging.

3.2 The L-VOD downscaling method

The 5-km resolution L-VOD is estimated from the $L-VOD_{5km\_NNR}$ by injecting spatial details from the AGB_{5km} using the MF-MRA method by the following equation:

$$L-VOD_{5km} = L-VOD_{5km\_NNR} + g \times (AGB_{5km} - AGB_{5km\_Low\_Pass}) \quad (1)$$

where $L-VOD_{5km\_NNR}$ stands for the monthly L-VOD data at 5-km resolution using NNR method. To extract the low-frequency component of the AGB data ($AGB_{5km\_Low\_Pass}$), morphological filtering was applied to the 5-km resolution AGB (AGB_{5km}). In this study, we assume that both AGB_{5km} and ($AGB_{5km\_Low\_Pass}$) remain constant within each year. Thus, for a given year, the same annual AGB value is applied to all twelve months in the Eq. (1) to match the monthly L-VOD data. Spatial details in AGB ($AGB_{5km} - AGB_{5km\_Low\_Pass}$) were extracted and injected by g (see Eq. (2)), and subsequently added to the monthly $L-VOD_{5km\_NNR}$ to enhance its spatial resolution. As a result, the downscaled $L-VOD_{5km}$ is a monthly dataset.

The injection gains g in Eq. (1) is a pixel-wise injection gain, representing the contribution of annual AGB to each monthly L-VOD. A total of 84 gain maps (7 years × 12months) were obtained to downscale the 5-km resolution monthly L-VOD series over the 7-year period (2015–2021), with each monthly gain map computed based on the corresponding annual AGB, as described in Eq. (2).

$$g = \frac{L-VOD_{5km\_NNR}}{AGB_{5km\_Low\_Pass}} \quad (2)$$

Note that injection gains g contain uncertainties, because the $L-VOD_{5km\_NNR}$ is not the true 5-km L-VOD although $L-VOD_{5km\_NNR}$ could represent the spatial-temporal information of $L-VOD_{25km}$. To reduce the uncertainties of g and enhance the accuracy and robustness of $L-VOD_{5km}$, the injection gains g were iteratively optimized by maximizing the Pearson correlation coefficient (R) between the $L-VOD_{5km}$ and the AGB_{5km}, formally:

$$g = argR(L-VOD_{5km}, AGB_{5km}) \quad (3)$$

in each iteration, the updated $L-VOD_{5km}$ was recalculated using the new g, and the correlation with AGB_{5km} was re-evaluated. In the initial iteration, the maximum value of g across all pixels and all layers was extracted and defined as the initial g_{limit}. In each subsequent iteration, if a pixel's g exceeded the current g_{limit}, it was set equal to g_{limit}, i.e., $g = (g, g_{limit})$. After each iteration, g_{limit} was reduced by a fixed step of 0.01, i.e., $g_{limit} = g_{limit} - 0.01$. Iterations were continued until $\Delta R < 0.01$ (ΔR is defined as the difference in R between iterations). Formally, the stopping criterion is:

$$\Delta R = |R^k - R^{k-1}| < 0.01 \quad (4)$$

where R^k and R^{k-1} are the correlation coefficients at the k-th and $(k-1)$-th iterations, respectively, and R is correlation coefficient between the $L-VOD_{5km}$ and the AGB_{5km}.

https://doi.org/10.5194/essd-2026-193
Preprint. Discussion started: 26 May 2026

To illustrate the proposed method, we take the year 2017 as an example. The 2017 AGB data at 5-km resolution and its low-frequency component obtained by morphological filtering are assumed constant for all twelve months of 2017. Thus, for each month $m = 1,2,3,\ldots,12$, the downscaled L-VOD at 5-km resolution is calculated as:

$$L-VOD_{5km}^{2017,m} = L-VOD_{5km\_NNR}^{2017,m} + g^{2017,m} \times (AGB_{5km}^{2017,m} - AGB_{5km\_Low\_Pass}^{2017,m}) \quad (5)$$

where $L-VOD_{5km}^{2017,m}$ and $L-VOD_{5km\_NNR}^{2017,m}$ represent the downscaled and nearest neighbor resampled monthly L-VOD for month m, respectively. $g^{2017,m}$ is the injection gain map corresponding to month m. $AGB_{5km}^{2017,m}$ is the annual AGB at 5-km resolution; and $AGB_{5km\_Low\_Pass}^{2017,m}$ is its low-frequency component derived by morphological filtering.

3.3 Accuracy assessment

Our analysis involves two main aspects, namely the methodological accuracy of the downscaling and the evaluation of the 5-km product.

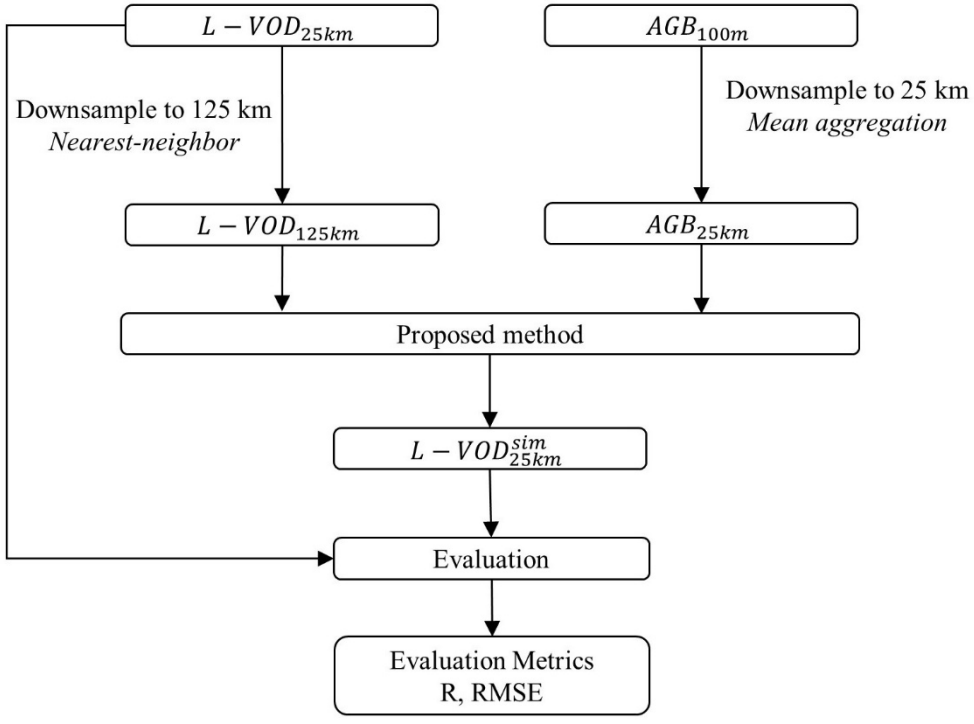

Figure 3. Schematic diagram of the validation approach. Methodological evaluation at 25-km resolution.

(i) Evaluation of the downscaling method. The approach for verifying the downscaling method is illustrated in Fig. 3. First, the original 25-km L-VOD (denoted as $L-VOD_{25km}$) is aggregated to 125-km spatial resolution via the nearest-neighbor algorithm (denoted as $L-VOD_{125km}$). In parallel, AGB_{25km} data is generated from the original AGB_{1km} by mean aggregation.

https://doi.org/10.5194/essd-2026-193
Preprint. Discussion started: 26 May 2026

Subsequently, both $L-VOD_{125km}$ and AGB_{25km} are utilized as inputs for the proposed method to generate a downscaled 25-km L-VOD, denoted as $L-VOD_{25km}^{sim}$. Thus, the original $L-VOD_{25km}$ acts as the reference benchmark, while $L-VOD_{25km}^{sim}$ represents the output of the downscaling method. Method performance was evaluated by computing the R and RMSE obtained from the comparison between the $L-VOD_{25km}^{sim}$ and $L-VOD_{25km}$. This validation framework has been adopted in previous studies and proven to be a reliable method for assessing core model performance, as documented by Merlin et al. (2008). The equations corresponding to these metrics are listed as follows:

$$R=\frac{Cov(L-VOD_{25km}^{sim},\ L-VOD_{25km})}{\sigma(L-VOD_{25km}^{sim})\sigma(L-VOD_{25km})} \tag{6}$$

$$RMSE=\sqrt{\frac{\sum(L-VOD_{25km}^{sim}-L-VOD_{25km})^2}{N}} \tag{7}$$

where Cov is the covariance and σ is the standard deviation. N is the sample size. Statistical significance was set at $p<0.05$.

(ii) Evaluation of $L-VOD_{5km}$ product. Regarding L-VOD datasets, no universal agreement has been reached on suitable reference VOD estimates from field observations or simulation models for validation purposes (Li et al., 2020). Hence, no single evaluation procedure is universally applicable, and instead diverse assessment strategies can be implemented under specific conditions. These conditions may include different vegetation regimes, such as grasslands and savannas (low-to-moderate cover) or tropical rainforests and boreal forests (dense cover), as well as specific sites affected by disturbances like deforestation and fire events (Grant et al., 2016; Tian et al., 2016; Xing et al., 2024).

The spatial correlation between $L-VOD_{5km}$ and AGB (Li et al., 2021) was used to assess the robustness of $L-VOD_{5km}$ datasets. It should be noted that the AGB dataset adopted here is the same as that used in the downscaling process, which provides spatial structural information for the downscaling of L-VOD. Therefore, this evaluation reflects spatial consistency between the $L-VOD_{5km}$ and AGB_{5km} rather than an independent accuracy validation. As a parameter characterizing microwave signal attenuation by vegetation, VOD displays spatial patterns across frequencies that closely resemble those of the IGBP global land cover classification (Konings et al., 2017). A set of VIs, including LAI and NDVI, were selected to be compared with $L-VOD_{5km}$, since they are commonly utilized as proxies for green vegetation coverage (Weber et al., 2020). Previous studies have extensively validated the representativeness of VOD by cross-comparing it with optical vegetation indices. (Grant et al., 2016; Lawrence et al., 2014; Li et al., 2020). Temporal correlations at the pixel level were calculated between $L-VOD_{5km}$ and these VIs. $L-VOD_{5km}$ spatiotemporal consistency with forest loss was examined, since Qin et al. (2021) observed a strong correlation between L-VOD dynamics and variations in forest loss within the Amazon Basin.

https://doi.org/10.5194/essd-2026-193
Preprint. Discussion started: 26 May 2026

Open Access Earth System Science Data Discussions

4 Results

4.1 Spatial pattern of the downscaled L-VOD data

In the process of downscaling, the spatial details being injected (i.e., the injection gains g defined in Eq. (1)) exhibit distinct patterns across various vegetation classes (Fig. 4a). In regions of tall, homogeneous vegetation, such as the Amazon, g is low. Our observation is in line with the saturation behavior of L-band signals, which occurs in dense vegetation canopies and at elevated values of above-ground biomass. In contrast, high g values appeared in zones dominated by short or heterogeneous vegetation, such as the Sahel. This pattern is consistent with the fact that the L-band signal has not yet reached saturation and is more sensitive to variations in AGB (Li et al., 2021). Vegetation type strongly influenced the median g (Fig. 4b). We observe that evergreen broadleaf forests show the lowest value of 1 (Fig. 4b), whereas croplands have the highest value of 4.05 (Fig. 4b).

The spatial distributions of both $L-VOD_{25km}$ (Fig. 4c) and the downscaled $L-VOD_{5km}$ (Fig. 4e) in August 2021 exhibited consistent patterns. Notably high $L-VOD_{5km}$ values were detected across tropical forests, with prominent examples being the Amazon and Congo basins; lower values were typical in short vegetation in tropical savannas and grasslands (e.g., Miombo woodlands in southern Africa); and very low values characterized arid and sparsely vegetated regions (e.g., northern Africa's Sahara and Australia's desert regions). In the median distributions across vegetation types, $L-VOD_{25km}$ reached the highest value in EBF at 0.78 (Fig. 4d). Similarly, $L-VOD_{5km}$ showed the highest value in EBF at 0.79 (Fig. 4f).

https://doi.org/10.5194/essd-2026-193
Preprint. Discussion started: 26 May 2026

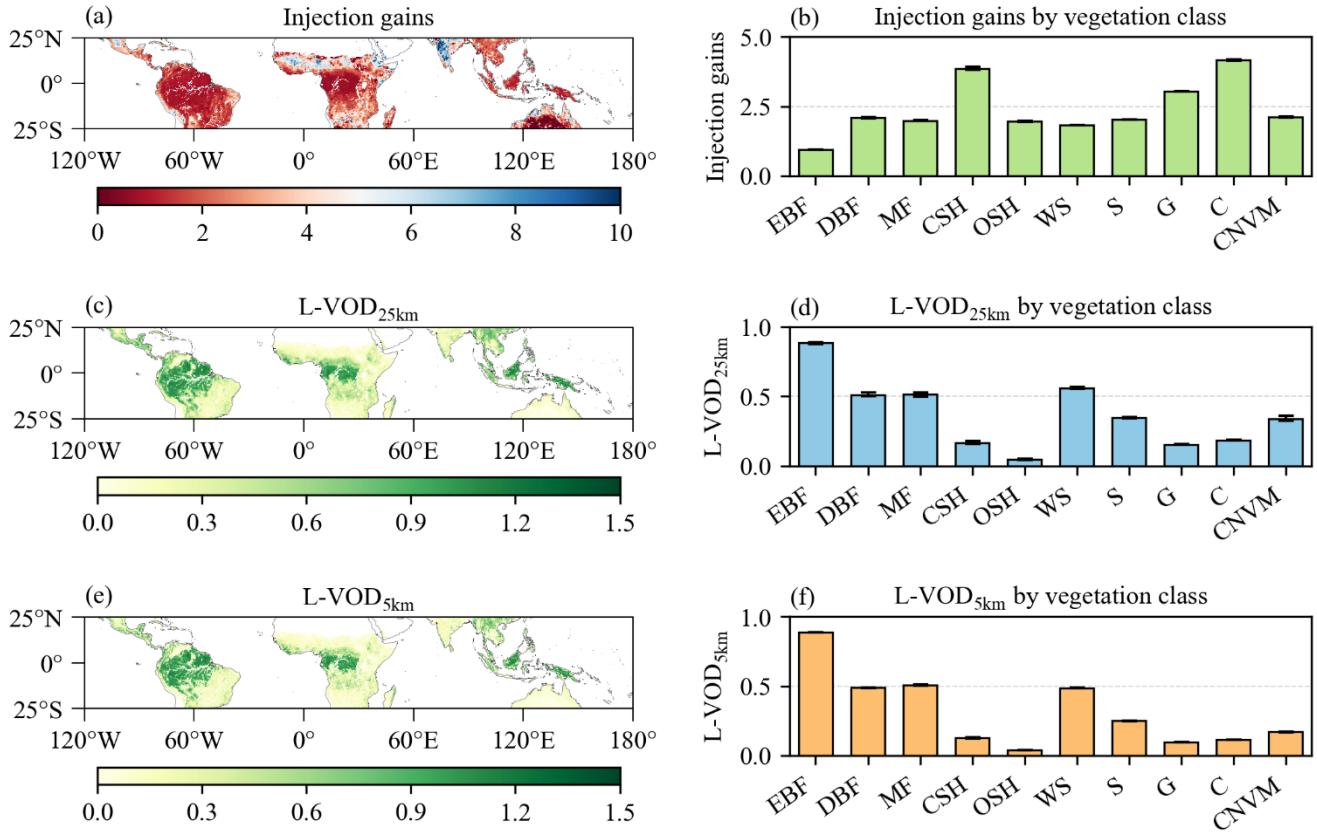

Figure 4. Spatial patterns and vegetation-class medians of the injection gains and L-VOD at 25-km and 5-km in August 2021. (a) Map of injection gains; (b) Median injection gains by vegetation class; (c) Map of $L-VOD_{25km}$ (d) Median $L-VOD_{25km}$ by vegetation class; (e) Map of $L-VOD_{5km}$ (f) Median $L-VOD_{5km}$ by vegetation class. Error bars denote the standard deviation of spatial variations.

Two representative sub-regions in Fig. 5(a, c) are provided as close-up views in Fig. 5b and Fig. 5d. In these areas, downscaled $L-VOD_{5km}$ reveals more spatial details than the $L-VOD_{25km}$. For example, in Region1 (Fig. 5b), the 5 km L-VOD exhibits alternating high- and low-value patches, which likely reflect smaller-scale variations in vegetation water content or canopy structure. This indicates that the downscaling method effectively enhances the detailed spatial information, which is critical for capturing more localized vegetation dynamics.

https://doi.org/10.5194/essd-2026-193
Preprint. Discussion started: 26 May 2026

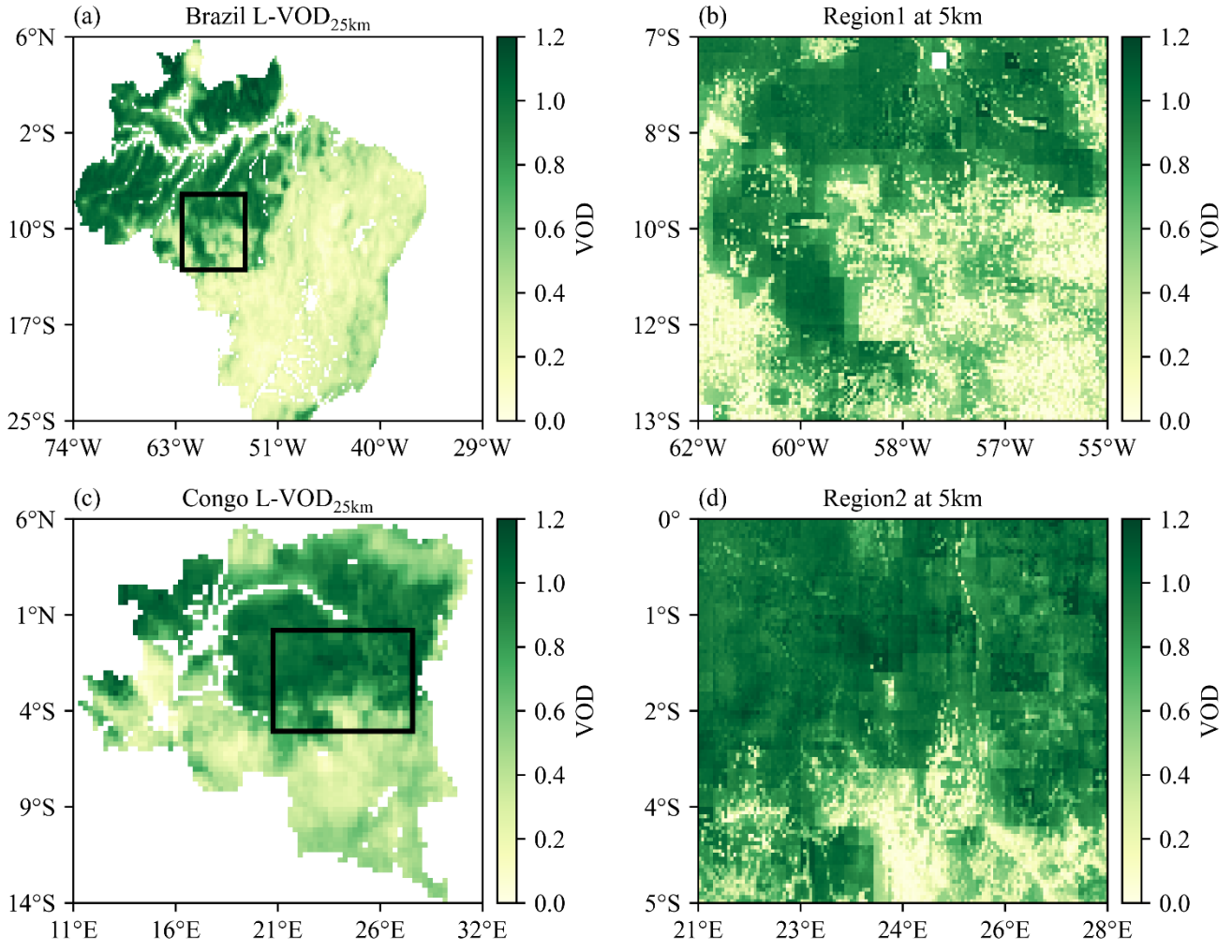

Figure 5. Detailed spatial information of the downscaled L-VOD in August 2021. (a) 25-km resolution L-VOD of Brazil. (b) 5-km resolution L-VOD of Region 1 (the black rectangular area in (a)). (c) 25-km resolution L-VOD of the Congo. (d) 5-km resolution L-VOD of Region 2 (the black rectangular area in (c)).

To further analyze the spatial details of $L-VOD_{5km}$, a small region of 2×2 $L-VOD_{5km}$ pixels was selected (Fig. 6a). $L-VOD_{5km}$ shows the enhanced pixel-level heterogeneity within the selected region, particularly in the southwestern part (Fig. 6e). The pixel value range within the study area expanded substantially from 0.74-1.00 (Fig. 6a) for the $L-VOD_{25km}$ to 0.05-1.01 for the $L-VOD_{5km}$ (Fig. 6e). This indicates that the downscaling process effectively enhances spatial details and reveals finer variations that are not captured at the $L-VOD_{25km}$.

The distributions of $L-VOD_{5km}$ (Fig. 6e) with AGB (Fig. 6f), NDVI (Fig. 6g), and CH (Fig. 6h) were found to be spatially similar within the selected 2×2 pixels region. For all four variables, high values are concentrated in the southwestern part and low values in the north-western part. $L-VOD_{5km}$ showed strong spatial correlations with AGB, NDVI, and CH, with

https://doi.org/10.5194/essd-2026-193
Preprint. Discussion started: 26 May 2026

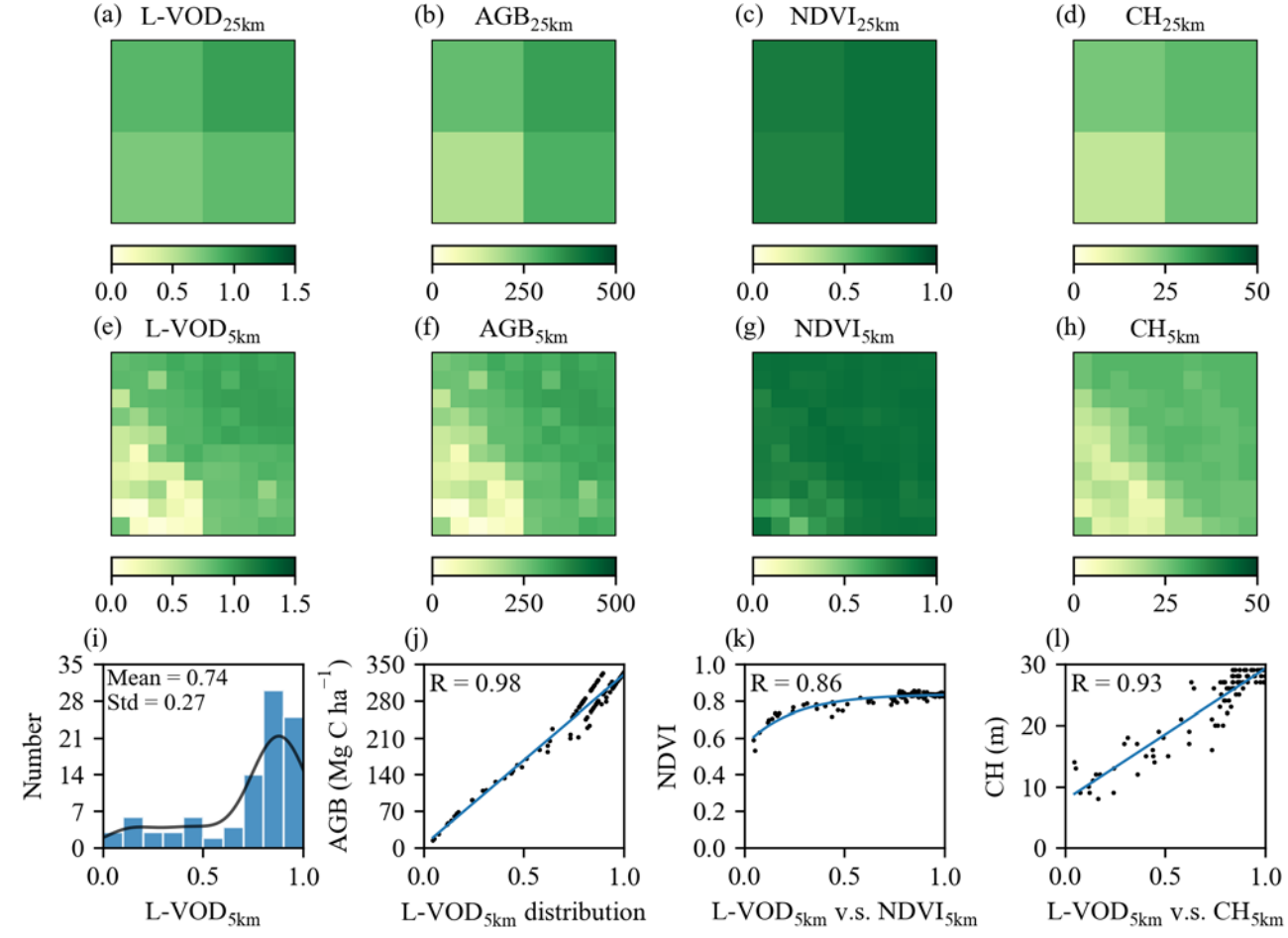

Figure 6. Detailed spatial information and relationships of L-VOD with AGB, NDVI and CH at 25-km and 5-km within four SMOS grid cells (corresponding to the locations of P1 in Fig. 1) in 2021. (a)$L-VOD_{25km}$; (b)AGB_{25km}; (c)$NDVI_{25km}$; (d)CH_{25km}; (e)$L-VOD_{5km}$; (f)AGB_{5km}; (g)$NDVI_{5km}$; (h)CH_{5km}; (i) Distribution of $L-VOD_{5km}$; (j) Scatter of $L-VOD_{5km}$ and AGB_{5km}; (k) Scatter of $L-VOD_{5km}$ and $NDVI_{5km}$, (l) Scatter of $L-VOD_{5km}$ and CH_{5km}.

4.2 Performance of the L-VOD downscaling method

The performance of the downscaling approach was assessed by calculating the R and $RMSE$ between the $L-VOD_{25km}^{sim}$ and the $L-VOD_{25km}$ for the year 2019. The R between the $L-VOD_{25km}^{sim}$ and $L-VOD_{25km}$ reached 0.95 and RMSE reached 0.11 (Fig.7a). The findings highlight the capacity of our framework to conserve the coarse-resolution patterns of the original L-VOD product, while maintaining reliability and precision in evaluations involving spatial scaling.

The superior performance was observed in forests compared to all other vegetation types, particularly in evergreen broadleaf forests (EBF), which exhibited the strongest correlation with R = 0.77 and $RMSE$ = 0.16 (Fig. 7c). Conversely, croplands

https://doi.org/10.5194/essd-2026-193
Preprint. Discussion started: 26 May 2026

Open Access Earth System Science Data Discussions

demonstrated the weakest correlation with R = 0.54 and $RMSE$ = 0.07 (Fig. 7c). Notably, although the model achieves the same R values between $L-VOD_{25km}^{sim}$ and $L-VOD_{25km}$ for both EBF and OSH at R =0.77 (Fig. 7b, f), it yields a lower RMSE in OSH with $RMSE$ =0.04 (Fig. 7f).

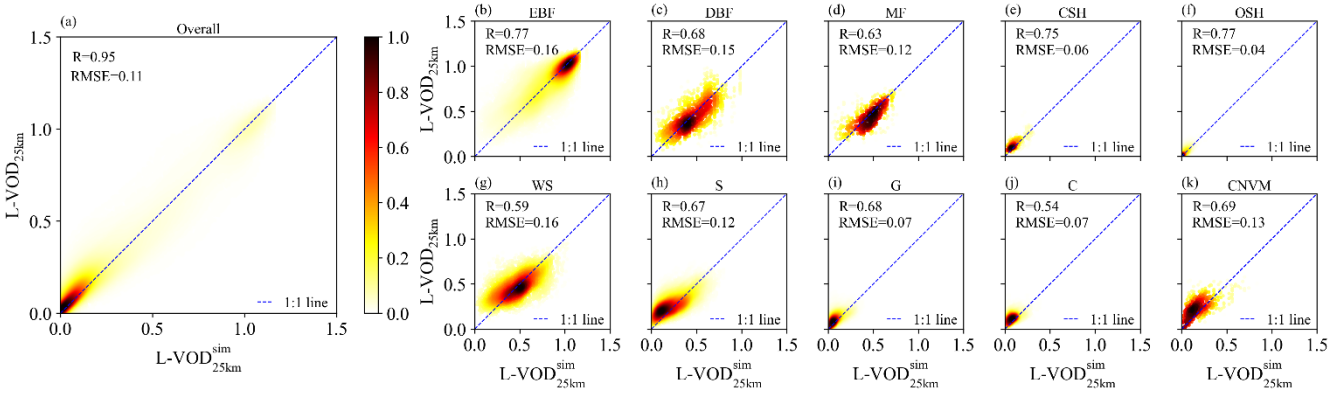

Figure 7. Scatter density plots evaluating the proposed method overall and by vegetation class. (a) Overall performance between $L-VOD_{25km}^{sim}$ and $L-VOD_{25km}$; (b-k) Performance by IGBP vegetation classes—EBF, DBF, MF, CSH, OSH, WS, S, G, C, and CNVM (in order).

4.3 The temporal and spatial assessment of downscaled L-VOD retrievals

Further analysis revealed that the downscaled $L-VOD_{5km}$ achieved an even higher spatial R of 0.91 with AGB_{5km} (Fig. 8b), relative to 0.87 (Fig.8a) in 2019. The improvement was also reflected by the coefficient of determination, with R^2 increasing from 0.81 to 0.86. This pattern was consistently observed across all other study years (Fig. A1). Meanwhile, the median of the pixel-wise temporal correlation $L-VOD_{5km}$ with AGB_{5km} reached R =0.9 (Fig. A2). This indicates that $L-VOD_{5km}$ effectively integrates fine-scale spatial structural information, while also capturing the temporal dynamics of vegetation growth. Furthermore, a universal improvement in R is observed across all land cover types. For instance, three major land cover categories—EBF, G, and CSH—exhibited R value improvements: EBF increased from 0.65 to 0.70 (Fig. 8c), G from 0.40 to 0.70 (Fig. 8c), and CSH from 0.651 to 0.81 (Fig. 8c). EBF shows the smallest improvement, while CNVM shows the largest. We analyzed the spatial correlation between $L-VOD_{5km}$ and AGB_{5km} in two representative regions: the Democratic Republic of the Congo (DRC, Fig. 8d) and Rondônia (Fig. 8e). In the region of DRC, $L-VOD_{5km}$ achieved a high R of 0.91 with AGB_{5km}, coupled with a low normalized root mean square error ($nRMSE$ =0.135) and a high R^2(0.83). In the Rondonia, $L-VOD_{5km}$ still maintained high correlation (R =0.92, R^2=0.84) with AGB_{5km} , though $nRMSE$ (0.27) was slightly elevated. These results demonstrate that $L-VOD_{5km}$ is capable of effectively capturing the subtle AGB gradients within local areas.

https://doi.org/10.5194/essd-2026-193
Preprint. Discussion started: 26 May 2026

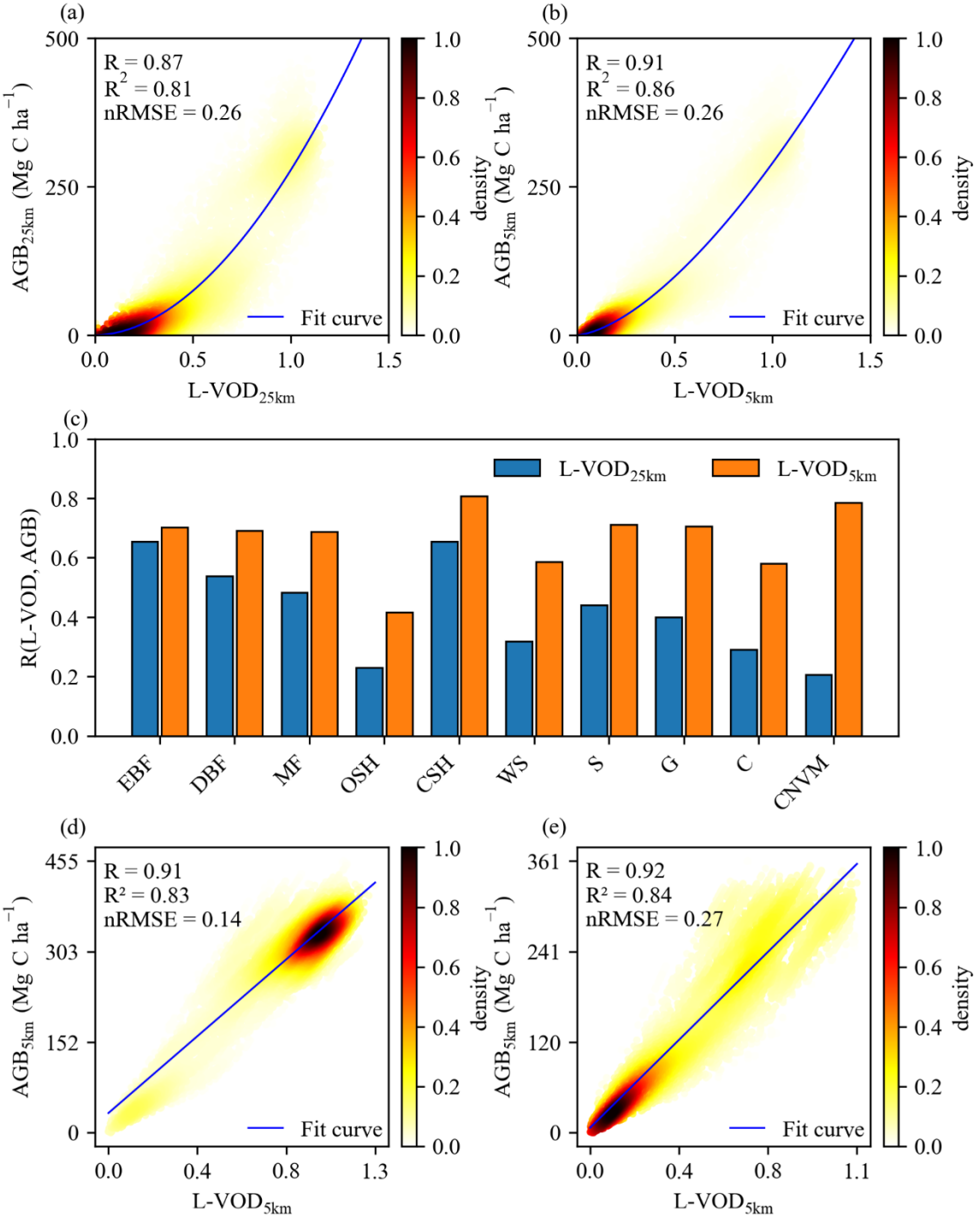

Figure 8. Spatial relationships between annual average L-VOD and AGB at 25-km and 5-km resolutions in 2019. (a) Density scatterplot between $L-VOD_{25km}$ and AGB_{25km}; (b) Density scatterplot between $L-VOD_{5km}$ and AGB_{5km}; (c) Comparison median value of R of L-VOD and AGB for each vegetation type; (d) Density scatterplot between $L-VOD_{5km}$ and AGB_{5km} in the DRC; (e) Density scatterplot between $L-VOD_{5km}$ and AGB_{5km} in Rondonia.

https://doi.org/10.5194/essd-2026-193
Preprint. Discussion started: 26 May 2026

The temporal correlations of L-VOD with LAI remained at a comparable level before and after downscaling (Fig. 9a, b), suggesting that our downscaling approach maintains the temporal dynamics of the original L-VOD. This was indicated by that the median R between the $L-VOD_{25km}$ and LAI was 0.57 (Fig. 9a), consistent with the 0.54 (Fig. 9b) correlation between
325 $L-VOD_{5km}$ and LAI. This was further confirmed by the similar values of temporal correlation between LAI, $L-VOD_{5km}$ and $L-VOD_{25km}$ over different vegetation types (Fig. 9c). For example, in grasslands, R was 0.7 for $L-VOD_{25km}$ and 0.66 for $L-VOD_{5km}$ (Fig. 9c). A strong similarity was observed between the spatial patterns of L-VOD—NDVI temporal correlation (Fig. A3) and that of LAI. In general, $L-VOD_{5km}$ correlated better with NDVI (R = 0.57) than with LAI (R = 0.54).

https://doi.org/10.5194/essd-2026-193
Preprint. Discussion started: 26 May 2026

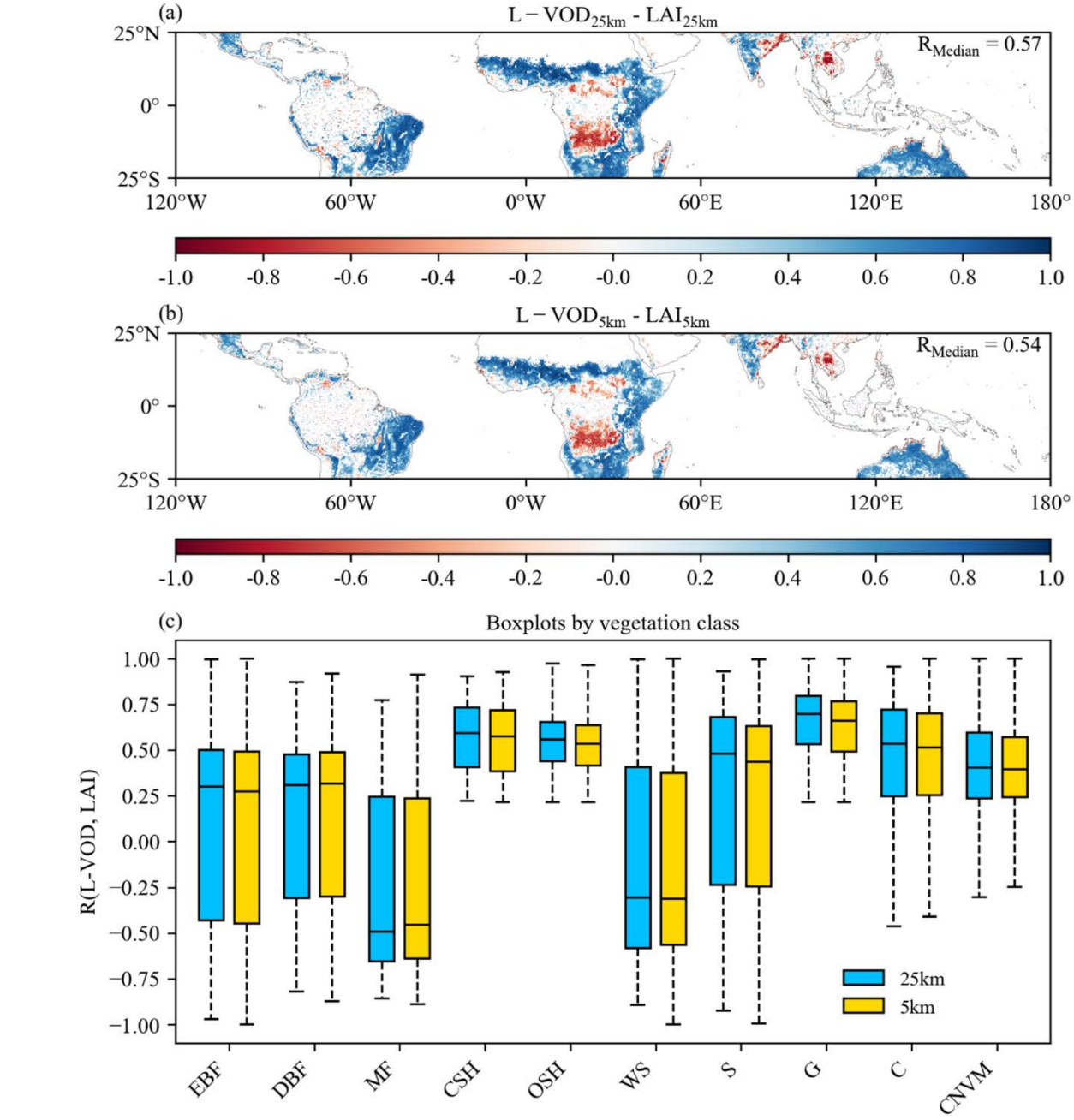

Figure 9. Spatially distributed temporal correlation coefficients (*R*) between monthly L-VOD and LAI from 2015 to 2021 at 25-km resolution (a) and at 5-km resolution (b). (a) and (b) blank areas represent pixels that were filtered out by scene flags, as well as desert regions and statistically non-significant correlations (p > 0.05).

We evaluate the $L-VOD_{5km}$ product with forest loss data, given that L-VOD has been shown to capture forest loss at 25-km resolution (Qin et al., 2021). The spatial distribution of forest loss area (Fig. A4) shows that the Brazilian Amazon contains

https://doi.org/10.5194/essd-2026-193
Preprint. Discussion started: 26 May 2026

areas of both high loss intensity and clear spatial clustering. We selected one grid cell for in-depth analysis in the Brazilian Amazon located at P2 (marked in Fig. 1), which experienced a 26% forest loss mainly concentrated in the north-western area during 2016. Within 25 km scale, $L-VOD_{5km}$ pixels exhibited a pronounced decline generally in the northwestern part of the cell (Fig. 10a). Correspondingly, the percentage (45%–64%) of forest loss area within the grid was also concentrated in the north-western region (Fig. 10b), indicating a strong spatial consistency between the changes in $L-VOD_{5km}$ and forest loss.

In terms of temporal dynamics, $L-VOD_{5km}$ effectively capture changes in forest loss. A 5km × 5km forest sample was selected at the site indicated by P2_1 in Fig. 10a, b. The L-VOD of this sample exhibited its largest decline between 2015 and 2016, decreasing from 0.77 to 0.72, a trend that continued into 2017 (Fig. 10c), while forest loss during the same period increased from 0% to 44% (Fig. 10c). This may be attributed to carbon losses captured by L-VOD across the Brazilian Amazon being likely influenced by additional drivers beyond deforestation in a given year (Li et al., 2022b) . For instance, forest degradation can lead to a decline in L-VOD, as verified by Qin et al. (2021).

Additionally, we compared $L-VOD_{5km}$ temporal dynamics with $NDVI_{5km}$ in the same sample (Fig. 10d). In 2015, $L-VOD_{5km}$ and NDVI are the same value 0.77, after the 2016 forest disturbance, $NDVI_{5km}$ dropped sharply from 0.77 to 0.60 but underwent rapid recovery in subsequent years (approaching 0.73 by 2021). In contrast, $L-VOD_{5km}$ also declined following the 2016 disturbance, but failed to recover rapidly thereafter. The lag in $L-VOD_{5km}$ was ascribed to the relatively slower recovery of both non-photosynthetic (woody) and photosynthetic (foliar) canopy biomass, in contrast to the more rapid canopy greenness response detected by $NDVI_{5km}$ (Jones et al., 2013). This demonstrates that the downscaled $L-VOD_{5km}$ not only captures vegetation disturbance but also reveals the lagged recovery of canopy biomass, effectively complementing the information provided by optical vegetation indices.

https://doi.org/10.5194/essd-2026-193
Preprint. Discussion started: 26 May 2026

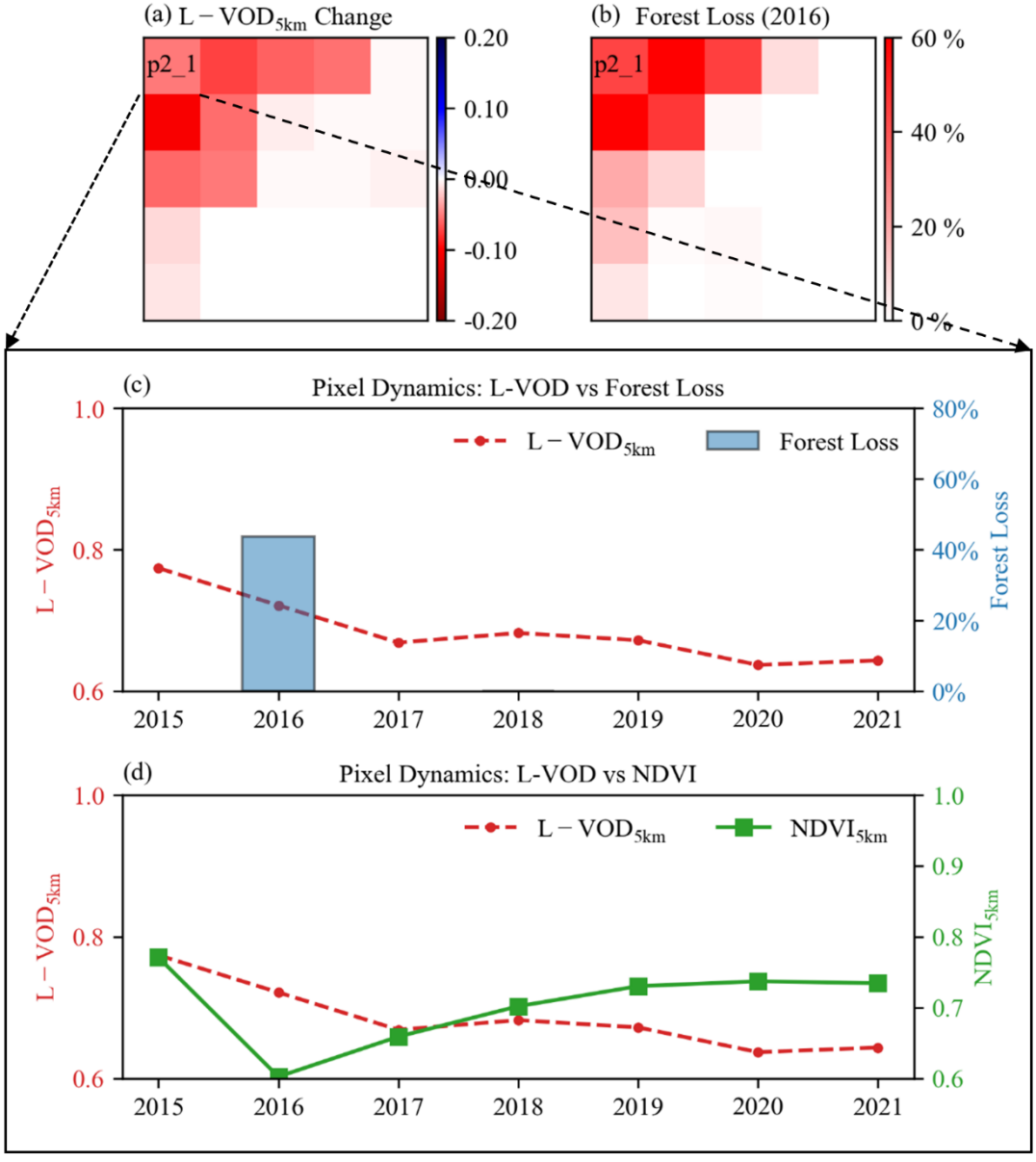

Figure 10. Spatiotemporal consistency analysis between downscaled L-VOD and forest loss within a 25-km grid cell in the Brazilian Amazon (corresponding to the locations of P2 in Fig. 1). (a) Change in L-VOD from 2015 to 2016 at 5-km resolution; (b) Forest loss percentages in 2016 at 5-km resolution; (c) Pixel-level (corresponding to the locations of P2_1 Fig. 9a, b) temporal dynamics of L-VOD (left axis) and forest loss area (right axis) from 2015 to 2021 at 5-km resolution; (d) temporal dynamics of L-VOD (left axis) and NDVI area (right axis) from 2015 to 2021 at 5-km resolution.

https://doi.org/10.5194/essd-2026-193
Preprint. Discussion started: 26 May 2026

5 Discussion

5.1 Overview of the strengths of the downscaling framework

This study introduces a framework for 5-km L-VOD estimation. Unlike statistical regression methods, our method sharpens $L-VOD_{5km}$ by injecting spatial structural features (e.g., texture, edges) from AGB_{100} data into the $L-VOD_{25km}$ baseline, rather than relying on auxiliary data absolute values. A direct jump to 1-km resolution (25×25 expansion) would generate unconstrained spatial details that lack support from $L-VOD_{25km}$, causing severe spatial distortions and loss of physical interpretability. Furthermore, our method is intended to integrate the respective advantages of the SMOC L-VOD products and CCI-AGB datasets: the temporal resolution of $L-VOD_{25km}$ and the spatial resolution of AGB_{100m}, and its potential benefits relative to conventional methods are explored in the following sections.

This method preserves the original temporal resolution of the VOD because it uses the VOD as a baseline for structural-feature injection. In comparison, the traditional downscaling approach is unable to eliminate the impacts of temporal discrepancies, since other auxiliary satellite datasets usually possess inconsistent observation times. (Hongtao et al., 2019). Furthermore, it does not require other ancillary satellite data that are susceptible to cloud contamination (such as optical/thermal infrared data), so the error in the $L-VOD_{5km}$ estimation process can be decreased.

The downscaling framework is to estimate higher-resolution VOD images by injecting the structural information from higher-resolution auxiliary datasets, instead of establishing explicit or implicit functions to convert pixel values from other satellite products (Bousquet et al., 2019; Mohite et al., 2022; Yan et al., 2025). Furthermore, our framework does not rely on a retrieval process, thereby avoiding the uncertainties within the radiative transfer models (RTMs) (Vergopolan et al., 2020).

To evaluate the performance of this approach, we compared it with the Gram–Schmidt adaptive (GSA) (Aiazzi et al., 2007), which is based on a linear transformation (Method B1). The proposed downscaling model achieved R of 0.95 Fig. 6a, whereas the GSA method showed a lower R at 0.86 (Fig. A5a). Fig. A5b, c presents a comparison of spatial details between the original L-VOD and the downscaled L-VOD products derived from two approaches across the study areas. It is evident that the downscaled L-VOD obtained using the method proposed in this study shows higher consistency in textural characteristics with the original L-VOD, as compared with the GSA method.

5.2 Uncertainties and perspectives

Despite the promising results, the framework still has some certain limitations. In the following part, we analyze the influences of these uncertainties and outline possible pathways for future improvement.

The injection gains g (see Eq. (2)), shown in Fig. 4a, a key parameter in our downscaling process, had uncertainties, because it is derived from the $L-VOD_{5km\_NNR}$ and $AGB_{5km\_Low\_Pass}$. Firstly, the $L-VOD_{5km\_NNR}$ is generated from the original L-VOD products using the NNR method. While this method effectively preserves the original values, it may cause the loss of textural details (Parker et al. 1983). Additionally, it should be noted that these L-VOD already contain inherent errors introduced by satellite sensor imaging and the retrieval algorithms (Hu et al., 2024). Secondly, a fundamental assumption in

https://doi.org/10.5194/essd-2026-193
Preprint. Discussion started: 26 May 2026

our methodology may introduce another potential source of error: the CCI-AGB data, which provide the static higher-resolution spatial structure, are assumed to be constant on a monthly basis within each year, as AGB represents a relatively stable structural component of vegetation, whereas the seasonal dynamics are primarily captured by VOD. This simplification may fail to capture intra-annual biomass dynamics, potentially leading to discrepancies when fused with monthly L-VOD observations. Furthermore, as the CCI-AGB dataset only characterizes forest biomass, its application to non-forest regions during the downscaling process may introduce additional errors in the extracted spatial features. Accordingly, future research efforts will prioritize the incorporation of high-resolution vegetation structural datasets with comprehensive coverage across diverse vegetation types, which is expected to mitigate such vegetation-type-related biases and improve the robustness of the downscaling framework across heterogeneous landscapes.

Direct validation of $L-VOD_{5km}$ is limited by the absence of consistent *in situ* observations or reliable model outputs (Li et al., 2020). We evaluated the temporal performance of $L-VOD_{5km}$ by employing two optical vegetation-related indices, namely NDVI and LAI, following the method proposed by Li et al. (2022a). Nevertheless, the variability discrepancy between $L-VOD_{5km}$ and VIs may stem from the fact that L-VOD represents vegetation water content (VWC), which conveys distinct information from optical VIs (NDVI shows greater sensitivity to leaf chlorophyll content, while LAI characterizes the overall density of vegetation). This could induce temporal lags and dynamic variations between their time series (Zhou et al., 2022). Acknowledging these limitations, we still believe that the chosen indicators are appropriate for evaluating $L-VOD_{5km}$ in present study, given that multiple studies have confirmed that strong spatiotemporal consistency between optical VIs and VOD, most notably in regions dominated by low-stature vegetation (Li et al., 2020; Li et al., 2022a; Li et al., 2021). Uncertainties associated with optical VIs may partially account for the weak correlation between these indices and $L-VOD_{5km}$ across portions of the study area (Forkel et al., 2013). Cloud interference and aerosol particles, for instance, often degrade data quality and introduce gaps in daily time series, yielding VIs that do not reliably reflect actual vegetation variability.

Recent technological advances are providing new opportunities to validate VOD more rigorously. First, field configurations using global navigation satellite systems (GNSS) can measure VOD using cost-effective sensors that receive microwave signals from navigation satellites. Second, land surface models are now including methods to model vegetation water content and thus estimate VOD globally at the same spatial scales as satellite measurements (Feldman, 2024). Therefore, the further development of these GNSS and model methods are needed such that satellite VOD can be more comprehensively validated.

6 Conclusion

In this study, SMOS L-VOD data were spatially enhanced from original 25-km resolution to 5-km over tropical regions using a downscaling L-VOD framework, which fuses higher-resolution structural information from AGB to enhance spatial details of the original SMOS L-VOD data.

In the absence of ground-based L-VOD observations, three complementary assessment approaches were implemented to examine the reliability of the 5-km products across tropical regions, as follows: (1) spatial evaluation using AGB (R=0.91,

https://doi.org/10.5194/essd-2026-193
Preprint. Discussion started: 26 May 2026

425 R^2 = 0.86), (2) pixel-level temporal consistency assessment using LAI and NDVI time series, and (3) disturbance response analysis based on forest loss data. Quantitative assessments demonstrate that the downscaled datasets effectively preserve the broad-scale spatial patterns of the original input (R =0.95 and $RMSE$ =0.11) while successfully fusing finer-scale structural information. The product also shows improved capacity in capturing localized variations in vegetation dynamics and demonstrates sensitivity to forest disturbances.

430 **Appendix A**

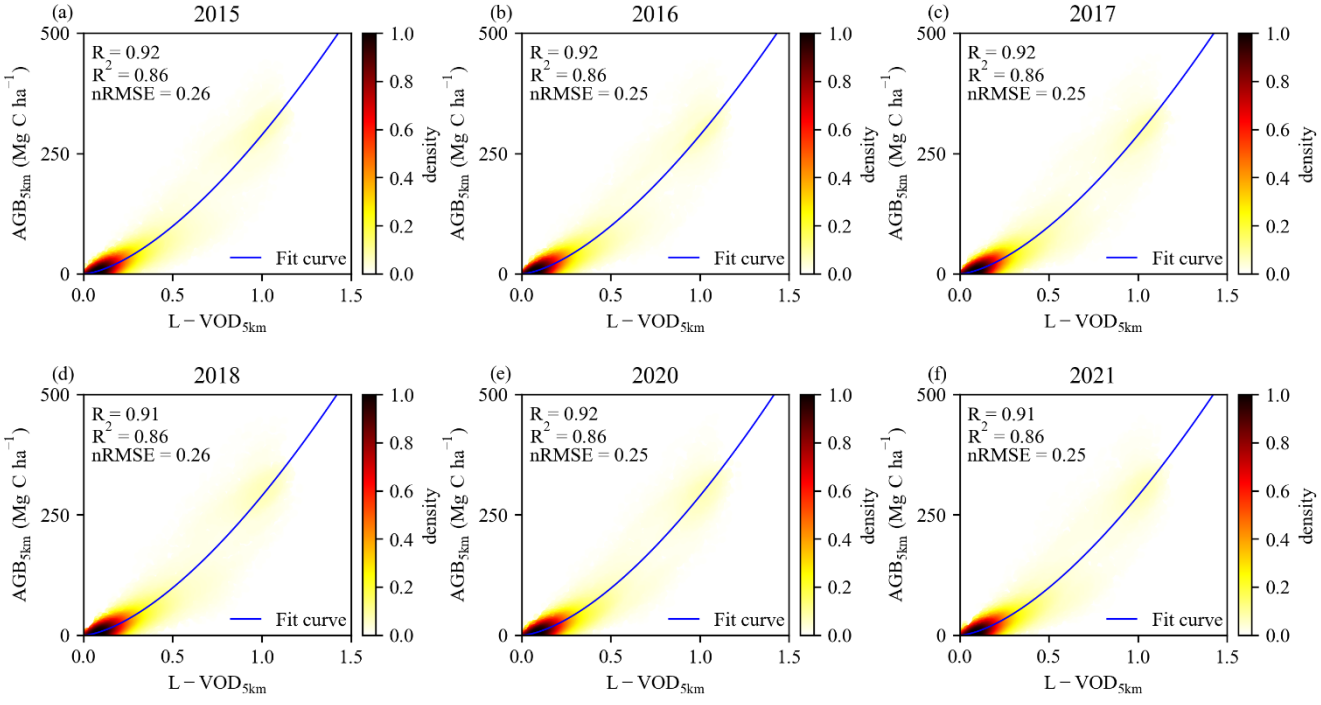

Figure A1. Correlations between yearly $L-VOD_{5km}$ and AGB_{5km} from 2015 to 2018, and in 2020 and 2021.

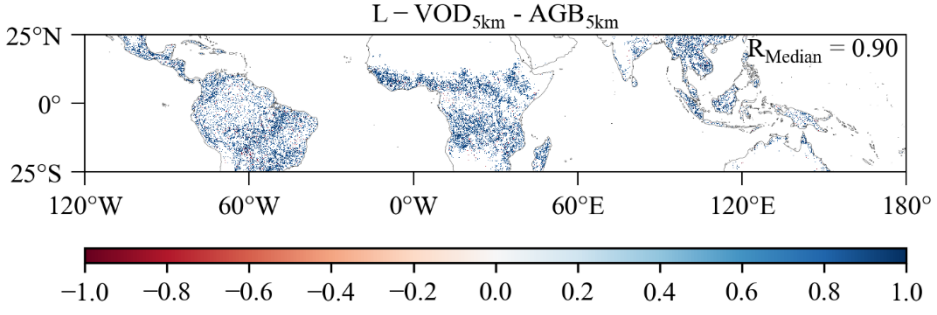

Figure A2. Spatial distribution of temporal correlation coefficients between $L-VOD_{5km}$ and AGB_{5km} over the 2015–2021 period.
435 **White areas indicate pixels with either missing valid data or statistically non-significant relationships (p > 0.05).**

https://doi.org/10.5194/essd-2026-193
Preprint. Discussion started: 26 May 2026

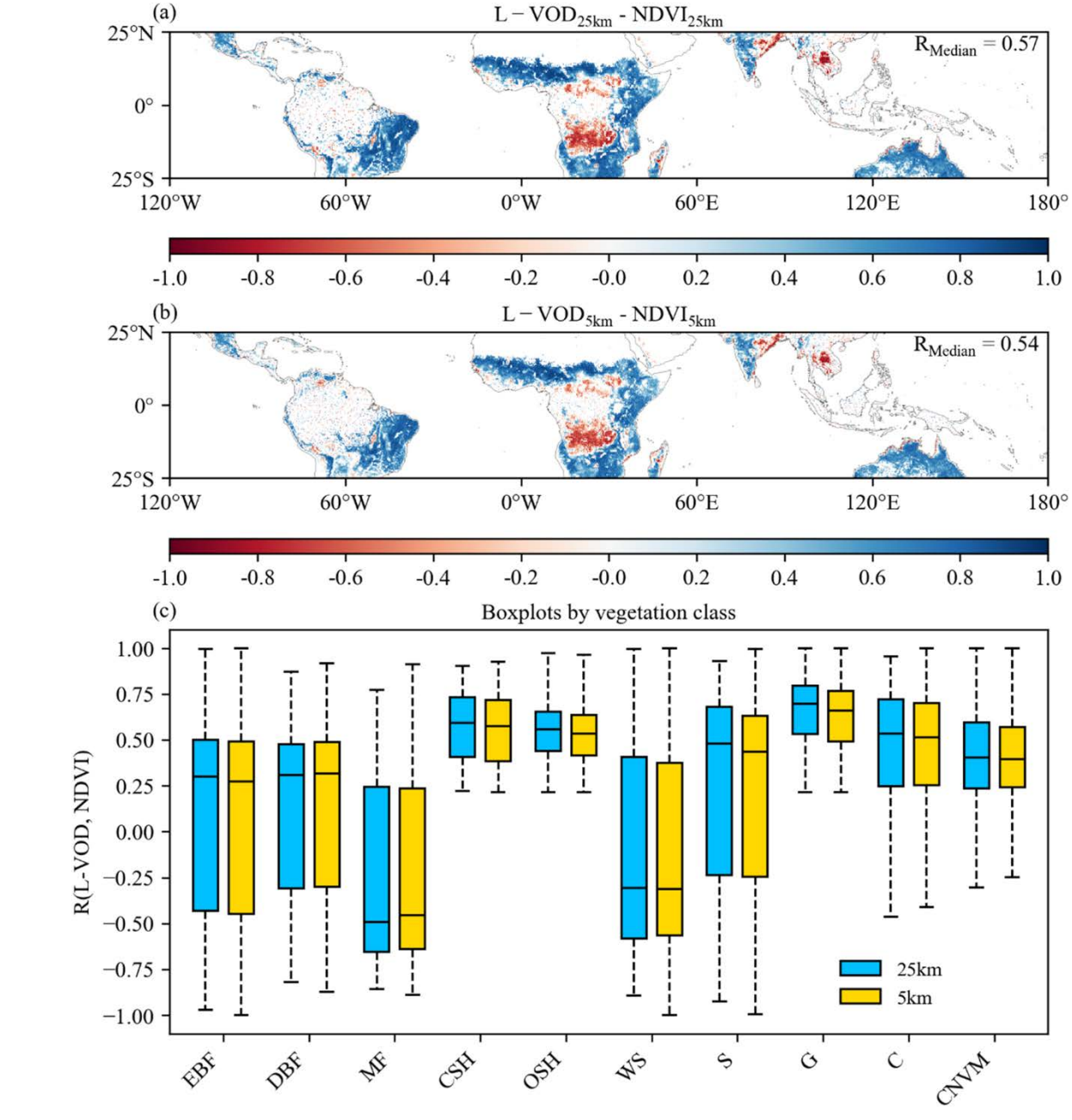

Figure A3. Pixel-wise temporal correlation (*R*) between monthly L-VOD and NDVI from 2015 to 2021 at 25-km resolution (a) and 5-km resolution (b); (c) Boxplots of correlations by IGBP vegetation class at 25-km and 5-km resolutions. (a) and (b) blank areas represent pixels that were filtered out by scene flags, as well as desert regions and statistically non-significant correlations (p > 0.05).

https://doi.org/10.5194/essd-2026-193
Preprint. Discussion started: 26 May 2026

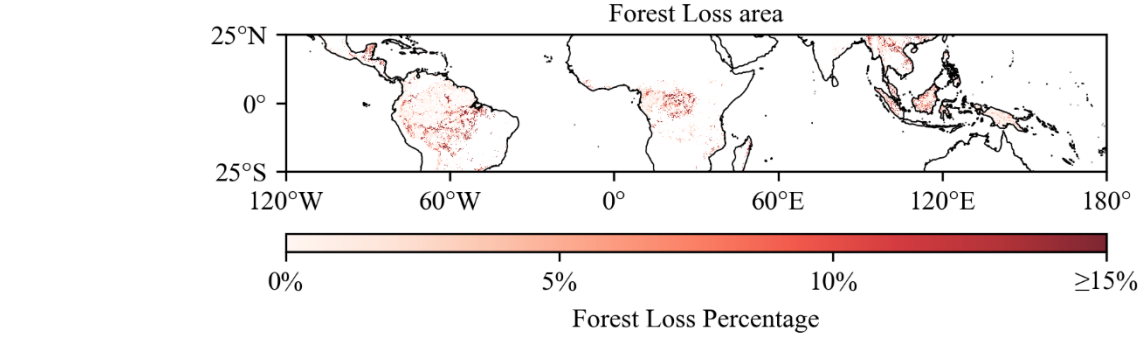

Figure A4. Maps of 5-km resolution forest loss area fraction for 2015–2021.

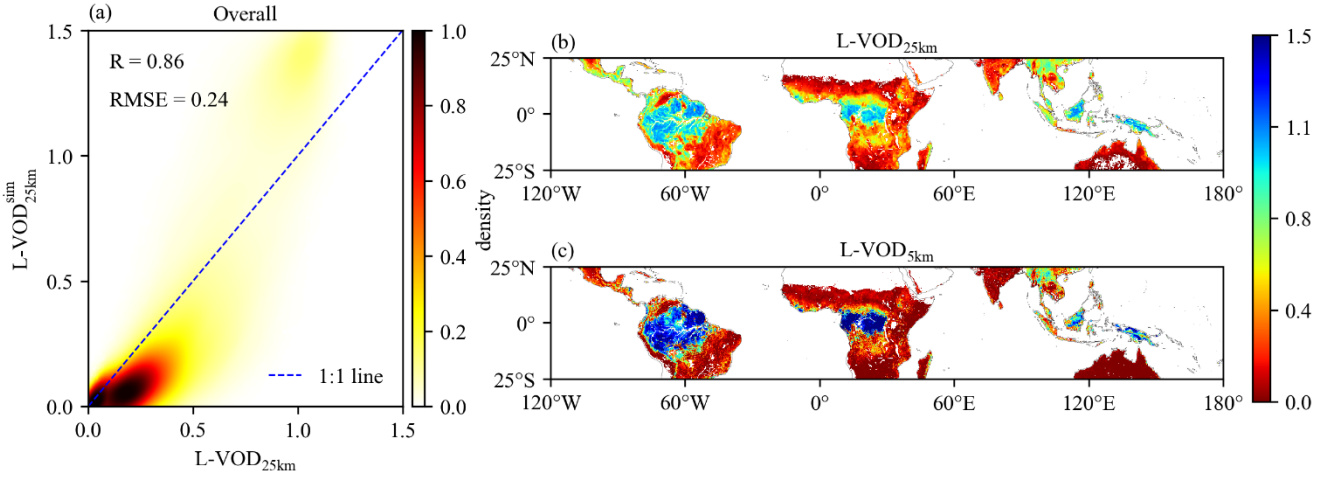

Figure A5. Results of GSA-based downscaling of L-VOD. (a) Density scatterplot comparing $L-VOD^{sim}_{25km}$ and $L-VOD_{25km}$; (b) Spatial pattern of the $L-VOD_{25km}$; (c) Spatial pattern of the $L-VOD_{5km}$.

Appendix B

Method B1. Gram-Schmidt Adaptive (GSA) Downscaling Method

The Gram-Schmidt Adaptive (GSA) method, a widely recognized pan-sharpening technique (Aiazzi et al., 2007), was employed as a benchmark to contextualize the performance of our developed downscaling method. In this study, we adapted the core principle of GSA—component substitution guided by multivariate regression—to the specific task of downscaling L-VOD data. The downscaling process involved three steps:

(1) Regression at Low Resolution: A multivariate regression model $L-VOD_{25km} = f(AGB_{25km})$ was established to learn the adaptive linear relationship between the two variables at the native 25-km scale.

(2) Spatial Component Synthesis: The derived regression coefficients were applied to the native AGB_{5km} to synthesize a higher-resolution spatial component I_{5km}, which inherited the fine spatial structure of AGB.

https://doi.org/10.5194/essd-2026-193
Preprint. Discussion started: 26 May 2026

(3) Fusion: The spatial details from I_{5km} were injected into an up-sampled version of the original L-VOD data via a component substitution scheme to generate the final $L-VOD_{5km}$.

Data availability

The pan-tropical 5-km monthly L-band vegetation optical depth dataset (2015–2021) is available at https://doi.org/10.11888/RemoteSen.tpdc.303391 (Shi and Fan, 2026).

Author contributions

JS and LF designed the experiments, and JS carried them out. LF, JL, LG, QY and SL provided related suggestions. LF, RF, PC, XL and SL reviewed and edited the text. JS prepared the manuscript with contributions from all co-authors.

Competing interests

The authors declare that none of the authors has any conflict of interest.

Financial support

This work was financially supported by the National Natural Science Foundation of China (42322103), the Chongqing Outstanding Youth Science Foundation (CSTB2024NSCQ-JQX0010).

Review statement

The review statement will be added by Copernicus Publications listing the handling editor as well as all contributing referees according to their status anonymous or identified.

References

Abbas, S., Wong, M. S., Wu, J., Shahzad, N., and Muhammad Irteza, S.: Approaches of satellite remote sensing for the assessment of above-ground biomass across tropical forests: Pan-tropical to national scales, Remote Sensing, 12, 3351, 2020.

Aiazzi, B., Baronti, S., and Selva, M.: Improving component substitution pansharpening through multivariate regression of MS $+ $ Pan data, IEEE Transactions on Geoscience and Remote Sensing, 45, 3230-3239, 2007.

https://doi.org/10.5194/essd-2026-193
Preprint. Discussion started: 26 May 2026

Boitard, S., Mialon, A., Mermoz, S., Rodríguez-Fernández, N. J., Richaume, P., Salazar-Neira, J. C., Tarot, S., and Kerr, Y. H.: Above ground biomass dataset from SMOS L band vegetation optical depth and reference maps, Earth System Science Data Discussions, 2024, 1-28, 2024.

Bousquet, E., Mialon, A., Rodríguez-Fernández, N. J., Mermoz, S., Bouvet, A., Merlin, O., and Kerr, Y. H.: Combining L-Band Radar and Smos L-Band Vod for High Resolution Estimation of Biomass, IGARSS 2019-2019 IEEE International Geoscience and Remote Sensing Symposium, 5508-5511,

Brandt, M., Wigneron, J.-P., Chave, J., Tagesson, T., Penuelas, J., Ciais, P., Rasmussen, K., Tian, F., Mbow, C., and Al-Yaari, A.: Satellite passive microwaves reveal recent climate-induced carbon losses in African drylands, Nature ecology & evolution, 2, 827-835, 2018.

Chaubell, J., Yueh, S., Dunbar, R. S., Colliander, A., Entekhabi, D., Chan, S. K., Chen, F., Xu, X., Bindlish, R., and O'Neill, P.: Regularized dual-channel algorithm for the retrieval of soil moisture and vegetation optical depth from SMAP measurements, IEEE Journal of Selected Topics in Applied Earth Observations and Remote Sensing, 15, 102-114, 2021.

Didan, K.: MOD13A1 MODIS/Terra Vegetation Indices 16-Day L3 Global 500m SIN Grid V006, NASA Land Processes Distributed Active Archive Center [dataset], http://doi.org/10.5067/MODIS/MOD13A1.006, 2015.

El Hajj, M., Baghdadi, N., Wigneron, J.-P., Zribi, M., Albergel, C., Calvet, J.-C., and Fayad, I.: First vegetation optical depth mapping from Sentinel-1 C-band SAR data over crop fields, Remote Sensing, 11, 2769, 2019.

Entekhabi, D., Njoku, E., O'Neill, P., Spencer, M., Jackson, T., Entin, J., Im, E., and Kellogg, K.: The soil moisture active/passive mission (SMAP), IGARSS 2008-2008 IEEE International Geoscience and Remote Sensing Symposium, III-1-III-4,

Fan, L., Wigneron, J.-P., Ciais, P., Chave, J., Brandt, M., Sitch, S., Yue, C., Bastos, A., Li, X., Qin, Y., Yuan, W., Schepaschenko, D., Mukhortova, L., Li, X., Liu, X., Wang, M., Frappart, F., Xiao, X., Chen, J., Ma, M., Wen, J., Chen, X., Yang, H., van Wees, D., and Fensholt, R.: Siberian carbon sink reduced by forest disturbances, Nature Geoscience, 16, 56-62, 10.1038/s41561-022-01087-x, 2022.

Feldman, A. F.: Emerging methods to validate remotely sensed vegetation water content, Geophysical Research Letters, 51, e2024GL110505, 2024.

Felton, A. J., Fisher, J. B., Hufkens, K., Purdy, A. J., Spawn-Lee, S. A., Duloisy, L. F., and Goldsmith, G. R.: Global estimates of the storage and transit time of water through vegetation, Nature Water, 3, 59-69, 2025.

Fernandez-Moran, R., Al-Yaari, A., Mialon, A., Mahmoodi, A., Al Bitar, A., De Lannoy, G., Rodriguez-Fernandez, N., Lopez-Baeza, E., Kerr, Y., and Wigneron, J.-P.: SMOS-IC: An alternative SMOS soil moisture and vegetation optical depth product, Remote Sensing, 9, 457, 2017.

Forkel, M., Carvalhais, N., Verbesselt, J., Mahecha, M. D., Neigh, C. S., and Reichstein, M.: Trend change detection in NDVI time series: Effects of inter-annual variability and methodology, Remote sensing, 5, 2113-2144, 2013.

https://doi.org/10.5194/essd-2026-193
Preprint. Discussion started: 26 May 2026

Frappart, F., Wigneron, J.-P., Li, X., Liu, X., Al-Yaari, A., Fan, L., Wang, M., Moisy, C., Le Masson, E., and Aoulad Lafkih, Z.: Global monitoring of the vegetation dynamics from the vegetation optical depth (VOD): A review, Remote Sensing, 12, 2915, 2020.

Friedl, M. A., Sulla-Menashe, D., Tan, B., Schneider, A., Ramankutty, N., Sibley, A., and Huang, X.: MODIS Collection 5 global land cover: Algorithm refinements and characterization of new datasets, Remote sensing of Environment, 114, 168-182, http://doi.org/10.5067/MODIS/MCD12C1.006, 2010.

Gevaert, A., Parinussa, R. M., Renzullo, L. J., van Dijk, A. I., and de Jeu, R. A.: Spatio-temporal evaluation of resolution enhancement for passive microwave soil moisture and vegetation optical depth, International Journal of Applied Earth Observation and Geoinformation, 45, 235-244, 2016.

Grant, J., Wigneron, J.-P., De Jeu, R., Lawrence, H., Mialon, A., Richaume, P., Al Bitar, A., Drusch, M., Van Marle, M., and Kerr, Y.: Comparison of SMOS and AMSR-E vegetation optical depth to four MODIS-based vegetation indices, Remote Sensing of Environment, 172, 87-100, 2016.

Hansen, M. C., Potapov, P. V., Moore, R., Hancher, M., Turubanova, S. A., Tyukavina, A., Thau, D., Stehman, S. V., Goetz, S. J., and Loveland, T. R.: High-resolution global maps of 21st-century forest cover change, science, 342, 850-853, doi: 10.1126/science.1244693, 2013.

Hongtao, J., Huanfeng, S., Xinghua, L., Chao, Z., Huiqin, L., and Fangni, L.: Extending the SMAP 9-km soil moisture product using a spatio-temporal fusion model, Remote Sensing of Environment, 231, 111224, 2019.

Hu, D., Wang, Y., Jing, H., Yue, L., Zhang, Q., Fan, L., Yuan, Q., Shen, H., and Zhang, L.: A global daily seamless 9-km Vegetation Optical Depth (VOD) product from 2010 to 2021, Earth System Science Data Discussions, 2024, 1-28, 2024.

Jackson, T. and Schmugge, T.: Vegetation effects on the microwave emission of soils, Remote Sensing of Environment, 36, 203-212, 1991.

Jiang, M., Shen, H., Li, J., and Zhang, L.: Generalized spatio-temporal-spectral integrated fusion for soil moisture downscaling, ISPRS Journal of Photogrammetry and Remote Sensing, 218, 70-86, 2024.

Jing, Y., Lin, L., Li, X., Li, T., and Shen, H.: An attention mechanism based convolutional network for satellite precipitation downscaling over China, Journal of Hydrology, 613, 128388, 2022.

Jones, M. O., Kimball, J. S., and Jones, L. A.: Satellite microwave detection of boreal forest recovery from the extreme 2004 wildfires in A laska and C anada, Global change biology, 19, 3111-3122, 2013.

Karthikeyan, L., Pan, M., Konings, A. G., Piles, M., Fernandez-Moran, R., Kumar, D. N., and Wood, E. F.: Simultaneous retrieval of global scale Vegetation Optical Depth, surface roughness, and soil moisture using X-band AMSR-E observations, Remote Sensing of Environment, 234, 111473, 2019.

Kerr, Y. H., Waldteufel, P., Wigneron, J.-P., Delwart, S., Cabot, F., Boutin, J., Escorihuela, M.-J., Font, J., Reul, N., and Gruhier, C.: The SMOS mission: New tool for monitoring key elements ofthe global water cycle, Proceedings of the IEEE, 98, 666-687, 2010.

https://doi.org/10.5194/essd-2026-193
Preprint. Discussion started: 26 May 2026

Konings, A. G., Piles, M., Das, N., and Entekhabi, D.: L-band vegetation optical depth and effective scattering albedo estimation from SMAP, Remote Sensing of Environment, 198, 460-470, 2017.

Konings, A. G., Piles, M., Rötzer, K., McColl, K. A., Chan, S. K., and Entekhabi, D.: Vegetation optical depth and scattering albedo retrieval using time series of dual-polarized L-band radiometer observations, Remote sensing of environment, 172, 178-189, 2016.

Lawrence, H., Wigneron, J.-P., Richaume, P., Novello, N., Grant, J., Mialon, A., Al Bitar, A., Merlin, O., Guyon, D., and Leroux, D.: Comparison between SMOS Vegetation Optical Depth products and MODIS vegetation indices over crop zones of the USA, Remote Sensing of Environment, 140, 396-406, 2014.

Lewis, S. L., Lopez-Gonzalez, G., Sonké, B., Affum-Baffoe, K., Baker, T. R., Ojo, L. O., Phillips, O. L., Reitsma, J. M., White, L., and Comiskey, J. A.: Increasing carbon storage in intact African tropical forests, Nature, 457, 1003-1006, 2009.

Li, X., Al-Yaari, A., Schwank, M., Fan, L., Frappart, F., Swenson, J., and Wigneron, J.-P.: Compared performances of SMOS-IC soil moisture and vegetation optical depth retrievals based on Tau-Omega and Two-Stream microwave emission models, Remote Sensing of Environment, 236, 111502, https://doi.org/10.1016/j.rse.2019.111502, 2020.

Li, X., Wigneron, J.-P., Fan, L., Frappart, F., Yueh, S. H., Colliander, A., Ebtehaj, A., Gao, L., Fernandez-Moran, R., and Liu, X.: A new SMAP soil moisture and vegetation optical depth product (SMAP-IB): Algorithm, assessment and inter-comparison, Remote Sensing of Environment, 271, 112921, 2022a.

Li, X., Wigneron, J.-P., Frappart, F., De Lannoy, G., Fan, L., Zhao, T., Gao, L., Tao, S., Ma, H., and Peng, Z.: The first global soil moisture and vegetation optical depth product retrieved from fused SMOS and SMAP L-band observations, Remote Sensing of Environment, 282, 113272, 2022b.

Li, X., Wigneron, J.-P., Frappart, F., Fan, L., Ciais, P., Fensholt, R., Entekhabi, D., Brandt, M., Konings, A. G., and Liu, X.: Global-scale assessment and inter-comparison of recently developed/reprocessed microwave satellite vegetation optical depth products, Remote Sensing of Environment, 253, 112208, 2021.

Liu, X., Wigneron, J.-P., Fan, L., Frappart, F., Ciais, P., Baghdadi, N., Zribi, M., Jagdhuber, T., Li, X., and Wang, M.: ASCAT IB: A radar-based vegetation optical depth retrieved from the ASCAT scatterometer satellite, Remote Sensing of Environment, 264, 112587, 2021.

Liu, X., Wigneron, J.-P., Wagner, W., Frappart, F., Fan, L., Vreugdenhil, M., Baghdadi, N., Zribi, M., Jagdhuber, T., and Tao, S.: A new global C-band vegetation optical depth product from ASCAT: Description, evaluation, and inter-comparison, Remote Sensing of Environment, 299, 113850, 2023.

Liu, Y. Y., De Jeu, R. A., McCabe, M. F., Evans, J. P., and Van Dijk, A. I.: Global long-term passive microwave satellite-based retrievals of vegetation optical depth, Geophysical Research Letters, 38, 2011.

Liu, Y. Y., van Dijk, A. I., Miralles, D. G., McCabe, M. F., Evans, J. P., de Jeu, R. A., Gentine, P., Huete, A., Parinussa, R. M., and Wang, L.: Enhanced canopy growth precedes senescence in 2005 and 2010 Amazonian droughts, Remote Sensing of Environment, 211, 26-37, 2018.

https://doi.org/10.5194/essd-2026-193
Preprint. Discussion started: 26 May 2026

Ma, H., Li, X., Zeng, J., Zhang, X., Dong, J., Chen, N., Fan, L., Sadeghi, M., Frappart, F., and Liu, X.: An assessment of L-band surface soil moisture products from SMOS and SMAP in the tropical areas, Remote Sensing of Environment, 284, 113344, 2023.

Merlin, O., Walker, J. P., Chehbouni, A., and Kerr, Y.: Towards deterministic downscaling of SMOS soil moisture using MODIS derived soil evaporative efficiency, Remote sensing of environment, 112, 3935-3946, 2008.

Mohite, J., Sawant, S., Pandit, A., and Pappula, S.: Spatial downscaling of vegetation optical depth using the modis and srtm observations, IGARSS 2022-2022 IEEE International Geoscience and Remote Sensing Symposium, 5870-5873,

Myneni, R., Knyazikhin, Y., and Park, T.: MYD15A2H MODIS/Aqua Leaf Area Index/FPAR 8-Day L4 Global 500m SIN G rid V006, NASA Land Processes Distributed Active Archive Center [dataset], http://doi.org/10.5067/MODIS/MYD15A2H.0 06, 2015.

Owe, M., De Jeu, R., and Holmes, T.: Multisensor historical climatology of satellite-derived global land surface moisture, Journal of Geophysical Research: Earth Surface, 113, 2008.

Owe, M., de Jeu, R., and Walker, J.: A methodology for surface soil moisture and vegetation optical depth retrieval using the microwave polarization difference index, IEEE Transactions on Geoscience and Remote Sensing, 39, 1643-1654, 2002.

Parker, J. A., Kenyon, R. V., and Troxel, D. E.: Comparison of interpolating methods for image resampling, IEEE Transactions on medical imaging, 2, 31-39, 2007.

Peng, J., Loew, A., Merlin, O., and Verhoest, N. E.: A review of spatial downscaling of satellite remotely sensed soil moisture, Reviews of Geophysics, 55, 341-366, 2017.

Piles, M., Entekhabi, D., and Camps, A.: A change detection algorithm for retrieving high-resolution soil moisture from SMAP radar and radiometer observations, IEEE Transactions on Geoscience and Remote Sensing, 47, 4125-4131, 2009.

Piles, M., Camps-Valls, G., Chaparro, D., Entekhabi, D., Konings, A. G., and Jagdhuber, T.: Remote sensing of vegetation dynamics in agro-ecosystems using smap vegetation optical depth and optical vegetation indices, 2017 IEEE International Geoscience and Remote Sensing Symposium (IGARSS), 4346-4349,

Porwal, S. and Katiyar, S. K.: Performance evaluation of various resampling techniques on IRS imagery, 2014 seventh international conference on contemporary computing (ic3), 489-494,

Potapov, P., Li, X., Hernandez-Serna, A., Tyukavina, A., Hansen, M. C., Kommareddy, A., Pickens, A., Turubanova, S., Tang, H., and Silva, C. E.: Mapping global forest canopy height through integration of GEDI and Landsat data, Remote Sensing of Environment, 253, 112165, https://doi.org/10.1016/j.rse.2020.112165, 2021.

Qin, Y., Xiao, X., Wigneron, J.-P., Ciais, P., Brandt, M., Fan, L., Li, X., Crowell, S., Wu, X., and Doughty, R.: Carbon loss from forest degradation exceeds that from deforestation in the Brazilian Amazon, Nature Climate Change, 11, 442-448, 2021.

Restaino, R., Vivone, G., Dalla Mura, M., and Chanussot, J.: Fusion of multispectral and panchromatic images based on morphological operators, IEEE Transactions on Image Processing, 25, 2882-2895, 2016.

https://doi.org/10.5194/essd-2026-193
Preprint. Discussion started: 26 May 2026

Santoro, M. and Cartus, O.: ESA Biomass Climate Change Initiative (Biomass_cci): Global datasets of forest above-ground biomass for the years 2010, 2015, 2016, 2017, 2018, 2019, 2020 and 2021, v5.01, NERC EDS Centre for Environmental Data Analysis [dataset], https://dx.doi.org/10.5285/bf535053562141c6bb7ad831f5998d77, 2024.

Shi, J. and Fan, L.: A pan-tropical 5-km monthly L-band vegetation optical depth dataset (2015-2021), National Tibetan Plateau Data Center [dataset], https://doi.org/10.11888/RemoteSen.tpdc.303391, 2026.

Skulovich, O., Li, X., Wigneron, J.-P., and Gentine, P.: Global L-band equivalent AI-based vegetation optical depth dataset, Scientific Data, 11, 10.1038/s41597-024-03810-2, 2024.

Stephens, B. B., Gurney, K. R., Tans, P. P., Sweeney, C., Peters, W., Bruhwiler, L., Ciais, P., Ramonet, M., Bousquet, P., and Nakazawa, T.: Weak northern and strong tropical land carbon uptake from vertical profiles of atmospheric CO2, Science, 316, 1732-1735, 2007.

Tian, F., Brandt, M., Liu, Y. Y., Verger, A., Tagesson, T., Diouf, A. A., Rasmussen, K., Mbow, C., Wang, Y., and Fensholt, R.: Remote sensing of vegetation dynamics in drylands: Evaluating vegetation optical depth (VOD) using AVHRR NDVI and in situ green biomass data over West African Sahel, Remote Sensing of Environment, 177, 265-276, 2016.

Tong, X., Brandt, M., Yue, Y., Horion, S., Wang, K., Keersmaecker, W. D., Tian, F., Schurgers, G., Xiao, X., and Luo, Y.: Increased vegetation growth and carbon stock in China karst via ecological engineering, Nature sustainability, 1, 44-50, 2018.

Tong, X., Brandt, M., Yue, Y., Ciais, P., Rudbeck Jepsen, M., Penuelas, J., Wigneron, J.-P., Xiao, X., Song, X.-P., Horion, S., Rasmussen, K., Saatchi, S., Fan, L., Wang, K., Zhang, B., Chen, Z., Wang, Y., Li, X., and Fensholt, R.: Forest management in southern China generates short term extensive carbon sequestration, Nature Communications, 11, 10.1038/s41467-019-13798-8, 2020.

Vergopolan, N., Chaney, N. W., Beck, H. E., Pan, M., Sheffield, J., Chan, S., and Wood, E. F.: Combining hyper-resolution land surface modeling with SMAP brightness temperatures to obtain 30-m soil moisture estimates, Remote Sensing of Environment, 242, 111740, 2020.

Vreugdenhil, M., Navacchi, C., Bauer-Marschallinger, B., Hahn, S., Steele-Dunne, S., Pfeil, I., Dorigo, W., and Wagner, W.: Sentinel-1 cross ratio and vegetation optical depth: A comparison over Europe, Remote Sensing, 12, 3404, 2020.

Wagner, W., Blöschl, G., Pampaloni, P., Calvet, J.-C., Bizzarri, B., Wigneron, J.-P., and Kerr, Y.: Operational readiness of microwave remote sensing of soil moisture for hydrologic applications, Hydrology Research, 38, 1-20, 2007.

Wang, M., Fan, L., Frappart, F., Ciais, P., Sun, R., Liu, Y., Li, X., Liu, X., Moisy, C., and Wigneron, J.-P.: An alternative AMSR2 vegetation optical depth for monitoring vegetation at large scales, Remote Sensing of Environment, 263, 112556, 2021.

Weber, M., Hao, D., Asrar, G. R., Zhou, Y., Li, X., and Chen, M.: Exploring the use of DSCOVR/EPIC satellite observations to monitor vegetation phenology, Remote Sensing, 12, 2384, 2020.

Wigneron, J.-P., Ciais, P., Li, X., Brandt, M., Canadell, J. G., Tian, F., Wang, H., Bastos, A., Fan, L., and Gatica, G.: Global carbon balance of the forest: satellite-based L-VOD results over the last decade, Frontiers in Remote Sensing, 5, 1338618, 2024.

https://doi.org/10.5194/essd-2026-193
Preprint. Discussion started: 26 May 2026

Wigneron, J.-P., Jackson, T., O'neill, P., De Lannoy, G., de Rosnay, P., Walker, J., Ferrazzoli, P., Mironov, V., Bircher, S., and Grant, J.: Modelling the passive microwave signature from land surfaces: A review of recent results and application to the L-band SMOS & SMAP soil moisture retrieval algorithms, Remote Sensing of Environment, 192, 238-262, 2017.

Wigneron, J.-P., Li, X., Frappart, F., Fan, L., Al-Yaari, A., De Lannoy, G., Liu, X., Wang, M., Le Masson, E., and Moisy, C.: SMOS-IC data record of soil moisture and L-VOD: Historical development, applications and perspectives, Remote Sensing of Environment, 254, 112238, 2021.

Xiao, Y., Li, X., Fan, L., De Lannoy, G., Peng, J., Frappart, F., Ebtehaj, A., de Rosnay, P., Xing, Z., and Yu, L.: Optimal model-based temperature inputs for global soil moisture and vegetation optical depth retrievals from SMAP, Remote Sensing of Environment, 311, 114240, 2024.

Xing, Z., Li, X., Fan, L., Frappart, F., Kim, H., Karthikeyan, L., Konkathi, P., Liu, Y., Zhao, L., and Wigneron, J.-P.: Seasonal-scale intercomparison of SMAP and fused SMOS-SMAP soil moisture products, Frontiers in Remote Sensing, 5, 10.3389/frsen.2024.1440891, 2024.

Xinyu, W., Shibo, F., and Jiahao, H.: Statistical Downscaling Method for Vegetation Optical Depth Based on NDVI, Journal of Applied Meteorological Science, 36, 33-42, 2025.

Yan, H., Wang, C., and Lu, X.: Downscaling of vegetation optical depth based on random forest using vegetation optical depth memory, Remote Sensing Letters, 16, 717-727, 2025.

Yang, H., Ciais, P., Frappart, F., Li, X., Brandt, M., Fensholt, R., Fan, L., Saatchi, S., Besnard, S., and Deng, Z.: Global increase in biomass carbon stock dominated by growth of northern young forests over past decade, Nature Geoscience, 16, 886-892, 2023.

Zhang, Y., Ciais, P., Wigneron, J.-P., Chave, J., Cong, N., Li, X., Yang, Y., and Saatchi, S.: How accurately does L band vegetation optical depth predict aboveground biomass?, International Journal of Applied Earth Observation and Geoinformation, 144, 10.1016/j.jag.2025.104931, 2025.

Zhou, Z., Fan, L., De Lannoy, G., Liu, X., Peng, J., Bai, X., Frappart, F., Baghdadi, N., Xing, Z., and Li, X.: Retrieval of high-resolution vegetation optical depth from Sentinel-1 data over a grassland region in the Heihe River Basin, Remote Sensing, 14, 5468, 2022.

Zotta, R.-M., Moesinger, L., Van Der Schalie, R., Vreugdenhil, M., Preimesberger, W., Frederikse, T., De Jeu, R., and Dorigo, W.: VODCA v2: Multi-sensor, multi-frequency vegetation optical depth data for long-term canopy dynamics and biomass monitoring, Earth System Science Data, 16, 4573-4617, 2024.